Second-order Phase Transition Behavior in a Polymer above the Glass Transition Temperature

Mitsuru Ishikawa,* Taihei Takahashi, Yu-ichiro Hayashi, Maya Akashi, Takayuki Uwada

Department of Chemistry, Faculty of Science, Josai University, 1-1 Keyaki-dai, Sakado, Saitama 350-0295, Japan

ABSTRACT: Glass transition was primarily considered to be not phase transition; instead, regarded as pseudo second-order phase transition due to its similarity to the ordinary second-order phase transition. Recent single-molecule spectroscopy developments have prompted re-investigating glass transition at the microscopic scale, confirming that the initial classification is correct and revealing that glass transition includes phenomena similar to second-order phase transition. They are characterized by microscopic collective polymer motion and discontinuous changes in temperature dependent relaxation times within a temperature window that includes the polymer calorimetric glass transition temperature. Generally, atom or molecule collective motion and discontinuous changes in physical quantities including relaxation times characterize critical phenomena associated with second-order phase transitions near specific temperatures. Thus, second-order phase transition phenomena are involved in polymer glass transition.

INTRODUCTION

Single-molecule spectroscopy (SMS) based on fluorescence[1] has opened a new era for exploring the molecular basis for cell biology,[1] analytical chemistry,[2] biochemistry and biophysics,[1,3] organic synthesis and drug discovery,[4] surface specific chemical reactions,[5] and polymer dynamics.[6–10] Now SMS has matured to where it offers a versatile tool to help advance many sciences and technologies. This progress has brought expectation that unexplored polymer dynamics may be found by SMS above the calorimetric glass transition temperature T_g and below the melting point T_m, typically T_g + 10–20 K. This state above T_g is generally known as metastable or super-cooled liquids,[11] regardless of polymers or monomers, in contrast to stable liquids above T_m. Molecular level understanding regarding the extraordinarily increased relaxation times τ_R by ten or more orders of magnitude at T_g has long been among a major unsolved problem in physics and chemistry.[12,13] Our early challenge was to deepen glass transition understanding based on this fundamental query about extraordinarily increased τ_R and related phenomena. The present work has been motivated by our earlier studies regarding SMS and time-resolved fluorescence spectroscopy using viscosity-sensitive fluorescence probes.[6, 7, 14, 15]

Before specifically considering present article challenge, we review temperature-dependent entropy S, heat capacity C_p, and glass forming material viscosity η, to show how the challenge is related to phase transition phenomena at the glass transition. Glass transition differs phase transition but was classified into pseudo second-order phase transition[16] due to the following similarities.

Thus, *second-order phase transition behavior* in the present article presents phenomena similar to second-order phase transition.
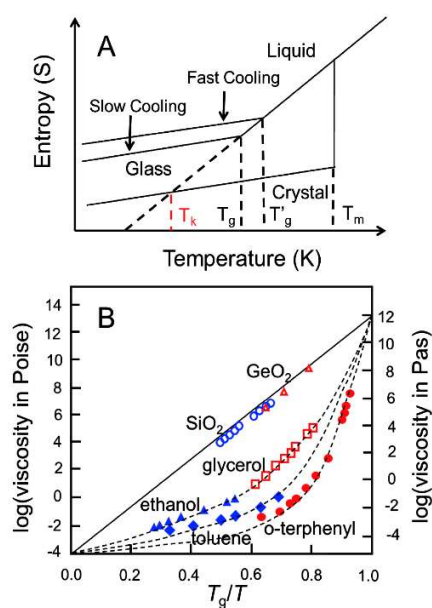
Figure 1. Glass transition fundamentals. (A) Temperature dependent entropy for glass forming materials including monomers and polymers, showing four important temperatures: melting point T_m, cooling-rate dependent glass transition temperatures T_g and T'_g, and Kauzmann temperature T_k; **(B)** Simplified Angel plot. **(A)** was adapted from an article (https://www.jps.or.jp/books/_gakkaishi/2016/05/71–0570fushigi_09.pdf.) by the Physical Society of Japan. **(B)** was adapted from ref 20.

1. Glass transition is not first-order phase transition but exhibits second-order phase transition behavior in the sense that liquid S profile joins the glass profile at T_g. Figure 1A shows that temperature dependent S continues from liquid to glass state without discontinuity at T_g, although the slopes differ either side of T_g.

2. Discontinuous change in temperature-dependent C_p suggests glass transition to be a type of second-order phase transition. Temperature dependent $C_p = T(\partial S/\partial T)_p$ has been evaluated by differential scanning calorimetry (DSC) to identify T_g, where a single staircase step in ΔC_p occurs, due to the discontinuous change in $(\partial S/\partial T)_p$ between liquid and glass state. The transformation interval ΔT associated with step ΔC_p is rather small, typically 10 K for glass forming materials.[17] Step ΔC_p or ΔC_p with C_p divergence, typically for liquid helium λ transition, characterizes second-order phase transition.[18, 19]

3. The Vogel–Fulcher–Tammann (VFT) equation (eq 1) suggests that η diverges at T_o similar to how order parameters such as magnetization do[19] near critical temperature T_c in second-order phase transition. Figure 1B shows an Arrhenius profile for η temperature dependence for glass forming materials sometimes called Angell plot.[20] Non-linear, or non-Arrhenius Angell plot curves fit the VFT relationship for η between T_g and $T_g + 50$ K[17] by

$$\log\left(\eta/\eta_\infty\right) = B/\left(T - T_o\right), \qquad (1)$$

where η_∞ is the limiting viscosity at infinite temperature, T_o is the Vogel temperature (several tens K below T_g,[17] and B and T_o are empirical parameters fitted from experimental observations. Actually, no one has experimentally observed η divergence sufficiently below T_g, very close to T_o beyond the Angel plot.

We learn further glass transition fundamentals to understand present article backgrounds. Figure 1A includes liquid and crystal separation below T_m, glass formation at T_g, and cooling-rate dependent T_g and T'_g; the difference between them can be 3–5 K on changing cooling rate by an order of magnitude.[11] Although cooling-rate dependence for T_g repels glass transition being a phase transition, glass transition exhibits second-order phase transition behavior, as exemplified above three representative instances.

Figure 1A also suggests another second-order phase transition behavior, showing that we can expect temperature to be crossed by the crystal and extrapolated liquid lines called the Kauzmann temperature T_k. Below T_g, the extrapolated liquid line falls beneath the crystal line, violating a thermodynamic fundamental that crystal entropy should be lower than that of liquid. Surprisingly, T_o is close to T_k for many glass forming materials,[11, 17] typically $0.9 < T_k/T_o < 1.1$.[11] Hence, T_k should be a real rather than imaginary temperature with substantial physical validity. The physics behind $T_o \approx T_k$ is challenging to address theoretically[21] and experimentally,[13] and hence to understand glass transition, but it is outside the present article scope.

Temperature dependent S, C_p, and η for glass forming materials thus offers possibilities to observe second-order phase transition behavior above T_k, or near T_g. We further examine glass transition and second-order phase transition related concepts to provide more direct background for the present article:

1. Glass forming material τ_R rather than η in dielectric spectroscopy, and τ_R in α process;
2. Collective molecular motion and cooperatively rearranging region (CRR) near T_g; and
3. Critical phenomena associated with second-order phase transition.

Angle plots (Figure 1B) confirm that η for many glass forming materials at T_g converges on $\approx 10^{12}$ Pas. Additionally, τ_R is approximately proportional to η, that is $\eta \approx G_g \cdot \tau_R$, where G_g is the glass modulus, 10^9–10^{12} Pa.[17] In practice, $\tau_R \approx 100$ s is widely accepted for glass forming materials at T_g[11, 12] as $G_g = 10^{10}$ Pa and a common rule of thumb for glassware workers. These values for η and τ_R are widely known as glass transition dynamics criteria.

Rather than η measurement, temperature dependent τ_R or relaxation frequencies ω have generally been investigated by dielectric spectroscopy, which characterizes glass transition through the extraordinary slowdown of $\omega \approx 1/\eta$ near T_g. In dielectric spectroscopy, a single peak occurs at ω for liquid of glass-forming material above T_m, that is, one relaxation mechanism dominates. Cooling the liquid below the crossover temperature $T_{cross} \approx 1.2 T_g$, expected from mode-coupling theory (MCT),[9, 22] splits a single peak into faster and slower peaks. Dynamics characterized by the slower frequency is called α process and that characterized by the faster frequency is called β process. The α process exhibits non-Arrhenius behavior and disappears at T_g, whereas β process continues Arrhenius behavior below T_g.[11] The τ_R for α process, typically 0.1–1.0 s, at $T_g + 10$–20 K, is much slower (> 10^6-fold) than for β process at T_g.[17] Because our SMS technique lacked temporal resolution to detect β process, we only considered α process assigned to polymer main chain segmental motion[23] and characterized by cooperative nature.[17]

Collective or cooperative molecular motion results from the non-Arrhenius Angell plot. Surrounding molecules form an energy barrier that a molecule of interest must overcome to move away. This barrier increases with reducing temperature, that is, the surrounding molecules behave collectively to affect molecule movement. Thus, non-Arrhenius behavior for η or ω leads to cooperative, or collective motion for glass forming materials as α process, and ultimately contributes to extraordinary τ_R slowdown. In addition, distinct spatial domains develop along with α process slowdown, generating spatial heterogeneity in glass forming materials.[11] Heterogeneity size was estimated at 1–5 nm near T_g for many glass forming materials.[17, 20, 24] It is the size of CRR, or characteristic length ξ_α, that is, average CRR diameter.

Critical phenomena involving fluids near T_c are characterized by highly fluctuating density in collective molecular motion. This is well exemplified by the CO_2 critical

phenomena, which generate a change in transparency to turbid appearance near T_c, known as critical opalescence.[19] Thus, CO_2 molecules behave collectively to form clusters, ultimately with size beyond or close to visible light wavelengths, 400–700 nm.

Generally, vigorously fluctuating long-wavelength collective molecular motions in fluids near T_c characterizes critical phenomena which present discontinuous order parameter divergence (e.g., liquid helium C_p forming cusp shapes) and form long-range order characterized by correlation length divergence (e.g., critical opalescence in CO_2), both of which characterize second-order phase transition.[19]

Based on glass transition fundamentals (Figures 1A and 1B) and the basic concepts above described, we outline *three major findings* in the present article, demonstrating polymer second-order phase transition behavior above T_g, much higher than T_k.

1. Substantial evidence for poly(vinyl acetate) PVAC environment collective motion. This was derived from temperature dependent autocorrelation function $C(\tau)$ in cosine waveform evaluated from a highly fluctuating fluorescence trajectory $I_f(t)$ of single-molecule Cy3, whose fluorescence efficiency highly depends on surrounding viscosity.

2. Temperature window above T_g but below T_{cross} exhibiting distinct cosine waveforms for $C(\tau)$. This appeared beyond the known theoretical framework for glass transition and related phenomena, such as MCT.[12, 13]

3. Discontinuous transition in temperature dependent average relaxation time $<\tau_R>$. This was evaluated from $C_{av}(\tau)$ averaged over many $C(\tau)$, at each temperature. The discontinuous plot was cusp shaped.[19] However, no correlation length divergence in PVAC was observed. If something similar to critical opalescence occurred, excitation light scattering enhanced background light, seriously disturbing fluorescence measurement in SMS.

We selected PVAC due to its T_g above room temperature (20–25 °C) and below 40 °C suitable for the present temperature controlling setup (see *Instruments used for SMS* in *Materials and Methods*). Viscosity-sensitive Cy3 was used in SMS,[7] because its fluorescence quantum efficiency Φ_f increased with increasing solvent viscosity: Φ_f = 0.042 in fluid (297 K) and 0.94 in rigid (77 K) ethanol solution, respectively.[25]

The importance of the present work lies in clearly identifying second-order phase transition behavior for PVAC above T_g but below T_{cross} (*Point 2*). This was strongly supported by cosine waveforms in $C(\tau)$ (*Point 1*), and the discontinuous temperature-dependent $<\tau_R>$ profile (*Point 3*). Although glass-transition is not generally recognized as a phase transition, the three major findings provide definite evidence that glass transition includes second-order phase transition behavior above T_g as pseudo second-order phase transition.[16]
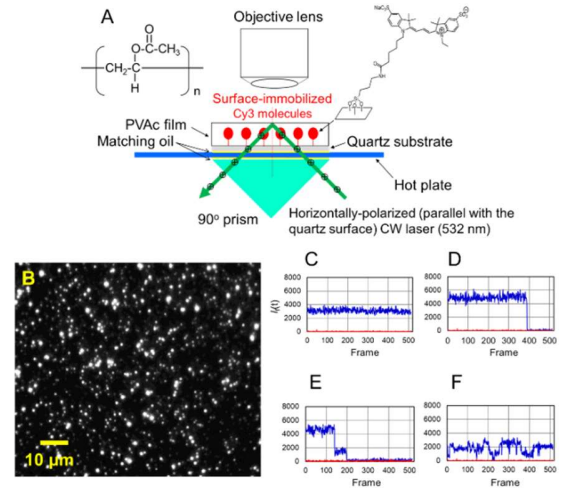
Figure 2. Single-molecule spectroscopy (SMS) fundamentals. (**A**) Experimental setup for SMS used in the present work: single Cy3 molecules covalently immobilized on a quartz surface with PVAC overlay, light microscope (shown as objective lens), quartz prism for horizontally polarized (parallel with the sample surface) evanescent illumination, and glass hot plate transparent in the visible region; (**B**) wide-field fluorescence image averaged over 512 frames (36 ms/frame) followed by background subtraction. Fluorescence trajectory $I_f(t)$ for single Cy3 molecules at room temperature (24.5 °C) showing (**C**) no photobleaching, (**D**) one-step photobleaching, (**E**) two-step photobleaching, and (**F**) substantial fluctuation.

*RES*ULTS

Major findings and others, overview

Figure 2A shows the SMS setup we employed to observe single-molecule Cy3 fluorescence images (Figure 2B) and $I_f(t)$ (Figures 2C–2F). We found stable, stepwise photobleaching, and large fluctuation $I_f(t)$. Stepwise photobleaching shows a single-molecule event,[1] hence we observed single Cy3 molecules. More details about SMS fundamental observations are included in the subsequent section.

We also present three major findings outlined in *Introduction* in more detail with specific experimental observations in 1, 2, and 3. Also, 4, 5, and 6 support single Cy3 sensitivity to PVAC environment and glass transition. We examined 4, 5, and 6 in *Discussion* to dispel concerns about SMS application to glass transition research using surface-immobilized single molecule probes.

1. Temperature dependent $C(\tau)$ (Figures 3A–3F for heating and Figures S1A–S1F for cooling) included remarkable cosine waveforms, hence evidence for collective PVAC motion above T_g. Figures 4A and 4B and Tables S1A and S1B summarize classification for $C(\tau)$ waveforms and their occurrences at each temperature for heating and cooling, respectively. Collective motion was deduced from $C(\tau)$ using the generalized Langevin equation (GLE).[26] The cosine $C(\tau)$ derivation is described in *Discussion* and *Supporting Information* (SI). Specific sub-second and second frequencies in power spectrum $J(\nu)$ (Figures 3A–3F and S1A–S1F), that is, the Fourier transform of $C(\tau)$, were compared with mechanical and dielectric PVAC

spectroscopy observations (Figures S2A and S2B) to explore the frequency origins in $J(v)$ in *Discussion*.

2. Cosine $C(\tau)$ was clearly observed in a temperature window between T_g and T_{cross}, where there was no applicable microscopic theory for glass transition. This temperature window was determined by temperature dependent $J_{av}^{max}(v)$ (Figures 5A and 5B), that is, the peak amplitude of $J_{av}(v)$ (Fourier transform of $C_{av}(\tau)$ evaluated by averaging twenty $C(\tau)$). Two sets of $J_{av}(v)$ for heating and for cooling are summarized in Figures S3A–S3L and Figures S4A–S4L, respectively.

3. Temperature dependent $<\tau_R>$ for heating and cooling exhibited discontinuous transition (Figures 5E and 5F, or equivalently Figures 5G and 5H) similar to a critical phenomenon cusp in second-order phase transition.[19] We used two sets of $C_{av}(\tau)$ (Figures S3A–S3L and Figures S4A–S4L) for heating and cooling, respectively to evaluate $<\tau_R>$. Temperature dependent $<\tau_R>$ details are included in *Discussion*.

4. PVAC overlay enhanced fluorescence intensities (2.16-fold) for single Cy3 molecules due to Cy3's viscosity sensitive fluorescence efficiency (Figures S5A and S5B),

5. No cosine $C(\tau)$ was observed without PVAC overlay, even in fluctuating $I_f(t)$ (Figures S6A–S6C).

6. Preferential horizontally polarized excitation (Figure 2A) was due to Cy3 absorption transition moment being highly oriented on a substrate surface at room temperature (23.8 °C) (Figures S7A and S7B) and even at an elevated temperature (56.3 °C) (Figures S7C and S7D).

Symbols in Figures 3A–3F, S1A–S1F, and S6A–S6C, for example T1 and T17, identify fluorescence spots in the video images mainly for authors' convenience to easily trace highlighted location on the original video images.

Observation of single Cy3 molecules

This section explains in advance SMS fundamental observations before investigating the major findings in the subsequent sections. Figure 2B shows a single molecule Cy3 fluorescence image with PVAC overlay at 24.5 °C. This image was processed by averaging 512 frames (36 ms/frame), followed by background subtraction. One hundred fluorescent spots were selected to evaluate photo-bleached spots in the 512-frame acquisition: 17–23% spots were photo-bleached with PVAC overlay, whereas 35–40% spots were photo-bleached without PVAC overlay at 22–25 °C. More than 70% spots were temporally stable (Figure 2C) with PVAC overlay. Single staircase photobleaching (Figure 2D) confirmed that the phenomenon was due to single Cy3 molecules, with rare (0.1% maximum) two-step photobleaching occurrences (Figure 2E). This means that one brighter fluorescent spot includes two Cy3 molecules. A few ($\approx$ 5%) highly fluctuating spots also present (Figure 2F). Ideally, we should follow the identical single Cy3 molecules from start to finish in all SMS measurement; however, photobleaching prohibited the ideal measurement. This is a fundamental SMS limitation noted in *Conclusions*.

Fluorescence intensity seemed to vary appreciably from spot to spot (Figure 2B). This was partly due to photo-bleached spots in the image acquisition and excitation light polarization, but mainly due to highly heterogeneous polymer structures. Excitation polarization effect on fluorescence intensity (*Point 6* in the previous section) is described in *Discussion*.

Temperature dependent single molecule fluorescence trajectories

This section investigates the first major finding: $C(\tau)$ cosine waveforms, one of the most important observations in the present article. No such waveform has previously been reported regarding glass transition researches to the best of the authors' knowledge.[7, 9, 11, 17, 20, 22] We derive cosine $C(\tau)$ from GLE and consider the $J(v)$ frequencies origin in *Discussion*. Cosine $C(\tau)$ is totally against the widely-known Kohlrausch–Williams–Watts (KWW) function $\exp[-(t/\tau_R)^\beta]$[11, 17, 20] used for α process analysis, where $0 < \beta \leq 1$ parameter expresses the τ_R distribution. However, averaging many single-molecule $C(\tau)$ made it possible to use the KWW function to compute τ_R (see *Relaxation time evaluation from autocorrelation functions*) from $C_{av}(\tau)$ by combining the KWW and cosine functions.

We observed $I_f(t)$ temporal fluctuations for twenty fluorescent spots that survived photo-bleaching in 512-frame video acquisition. Figures 3A–3F illustrate representative $I_f(t)$, $C(\tau)$, and $J(v)$ while heating 24.5–64.9 °C. A remarkable $C(\tau)$ cosine waveform appeared at 41.9 °C. Temperature dependent $C(\tau)$ waveform classification into Type I–V allowed us to identify a specific temperature window between 30 and 60 °C (the subsequent section for details). Temperatures were elevated step-by-step manner: 24.5, 28.3, 29.6, 32.0, 35.6, 37.8, 41.9, 45.4, 51.9, 56.4, 60.2, and 64.9 °C at 0.2–0.3 K/min. Figure 4A and Table S1A summarize occurrences for each $C(\tau)$ type at the above temperatures. Classification criteria for $I_f(t)$ are as follows: Type I for stable $I_f(t)$ and no specific peaks in $J(v)$, Type II for fluctuating $I_f(t)$ but not touching base line with a small (<0.10) single peak in $J(v)$, Type III for fluctuating $I_f(t)$ touching base line with a prominent (0.20<) single peak in $J(v)$, and Type IV for fluctuating $I_f(t)$ touching base line with a prominent (<0.20) single or multiple peaks in $J(v)$, and Type V for fluctuating $I_f(t)$ touching base line without prominent peaks (0.10<) in $J(v)$. Type V in $C(\tau)$ and $J(v)$ is similar to those of Type I. The increasing frequencies in $J(v)$ with increasing temperature motivated us to classify and select $C(\tau)$ in Figures 3A–3E and Figures S1A–S1E.
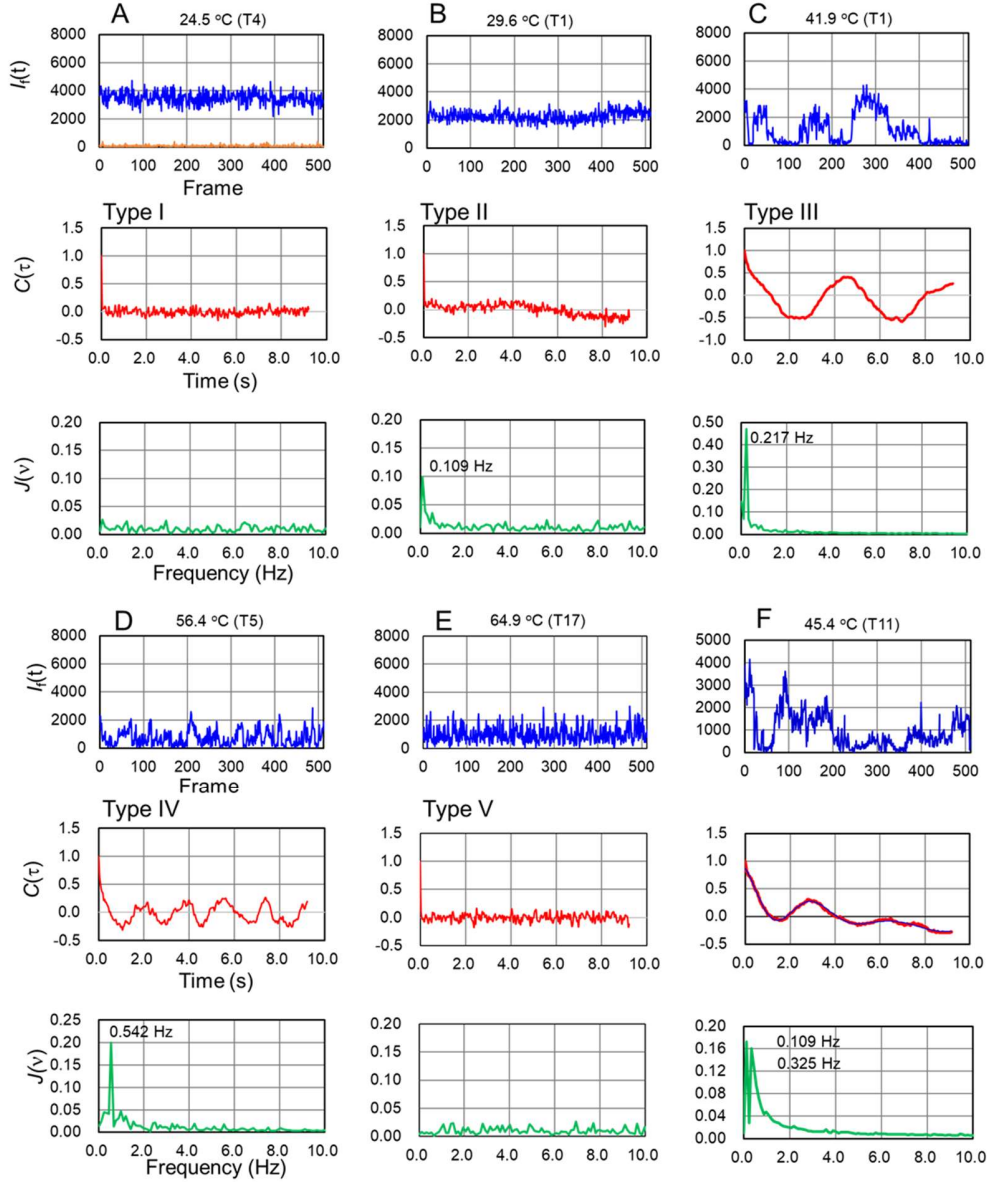
Figure 3. Temperature dependent representative fluorescence trajectories, $I_f(t)$; autocorrelation functions, $C(\tau)$; and power spectra, $J(v)$. They were observed from single Cy3 molecules with PVAC overlay from heating experiment (0.2 K /min) at (**A**) 24.5, (**B**) 29.6, (**C**) 41.9, (**D**) 56.4, (**E**) 64.9, and (**F**) 45.4 °C. Set (**F**) shows $C(\tau)$ damped oscillation (red curve), which was satisfactorily fitted with a fitting function (blue curve) $C(\tau) = C_0\exp(-t/C_1)\{C_2\cos(C_3t + C_4) + C_5\cos(C_6t + C_7) + C_8\cos(C_9t + C_{10}) + C_{11}\cos(C_{12}t + C_{13})\} + C_{14}$. Both curves coincide well with each other. The fitting function includes four cosine functions against immediate expectation from $J(v)$, two cosine functions including two distinct frequencies 0.109 and 0.325 Hz in $J(v)$. This is likely due to tailing in the 0.325 Hz spectrum, showing unresolved spectra contribution in $J(v)$. Labels Type I to Type V are for $C(\tau)$ classification; Figure 4A and Table S1A summarize each type occurrences. Video images generating these data were captured with horizontally polarized excitation and averaged over 512 frames (36 ms/frame) followed by background subtraction.

Figures 3A–3F include limited temperatures, because these figures are mainly to highlight the remarkable $C(\tau)$ cosine waveform at 41.9 °C. Specific sub-second frequencies were characterized by the prominent amplitude in each $J(v)$: 0.109 Hz (0.096), 0.217 Hz (0.472), and 0.542 Hz (0.200), where parentheses indicate the highest $J(v)$ value obtained at 29.6, 41.9, and 56.4, respectively. Sub-second frequencies were commonly observed in $J(v)$. Because $J(v)$ amplitudes can be a measure of *purity* in cosine waveforms, we compared the highest $J(v)$ 0.472 at 41.9 °C with amplitude 0.930 (0.977 Hz) computed by Fourier trans-

form of the noise-free and damping-free unitary cosine wave at 1 Hz (cos 2πt) with 36 ms bin time used to acquire all imaging data, with > 50% (0.472/0.930) purity for $C(\tau)$ in Figure 3C. To avoid possible misunderstandings that all observed $C(\tau)$ continued forever, Figure 3F shows $C(\tau)$ damped oscillation reproduced by the sum of cosine functions multiplied by a single exponential decay amplitude, which was classified into Type IV. Damped $C(\tau)$ oscillation was dominantly observed in Type III and IV.

Specific temperature window above T_g

This section examines the second major finding: a specific temperature window with $C(\tau)$ dominantly including cosine waveform. By heating single molecule samples 24.5–64.9 °C and then cooling 64.6–25.3 °C, we found a specific temperature window between 30 and 60 °C, including T_g = 36.5 °C (309.5 K) evaluated by DSC. These temperatures are considerably less than the crossover temperature T_{cross} predicted by MCT, $T_{cross} \approx 1.2 T_g$ = 371.4 K (98.4 °C).[11, 12] Thus, the temperature window characterized by highly fluctuating collective PVAC motions embodied by the $C(\tau)$ cosine waveform appears outside MCT but involves cooperative α process active zone.[17]
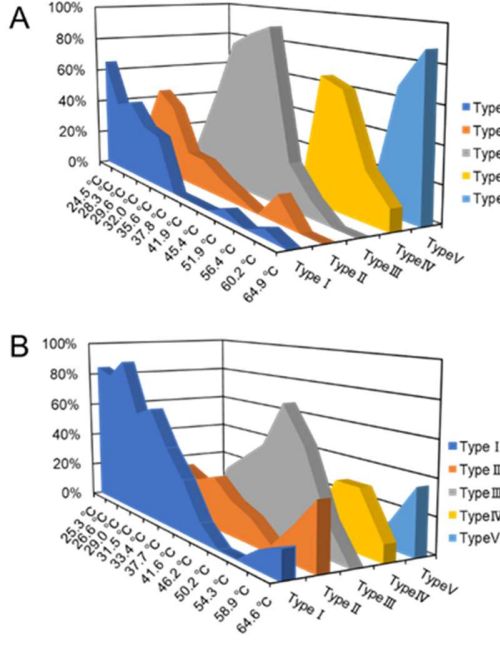

Figure 4. Autocorrelation $C(\tau)$ classification into six types for each observed temperature. Type I to Type V occurrences for (**A**) heating 24.5–64.9 °C (0.2 K/min) and (**B**) cooling from 64.6–25.3 °C (0.2–0.3 K/min) are summarized. Twenty fluorescent spots from single Cy3 molecules with PVAC overlay were collected at each temperature. Video images generating these data were captured with horizontally polarized excitation and averaged over 512 frames (36 ms/frame) followed by background subtraction.

Figures 3A–3E highlight remarkable temperature-dependent $C(\tau)$ waveforms from heating experiment at the selected temperatures. However, the waveforms were not always classified into Type I, for example at 24.5 °C. Figure 4A and Table S1A summarize twenty $C(\tau)$ classification (Type I–V) at each temperature. For example, $C(\tau)$ includes Type II, III, IV, and V occurrences at 56.4 °C. This wide diversity is not surprising, considering the intrinsically inhomogeneous polymer structure probed by SMS.

Figures 3A–3E also show representative $J(v)$, with highest amplitudes from 0.096 at 29.6 °C to 0.200 at 56.4 °C and maximum overall amplitude 0.472 at 41.9 °C. To ensure that this tendency was fundamental, we evaluated $C_{av}(\tau)$ by averaging twenty $C(\tau)$ waveforms survived from photobleaching and computed $J_{av}(v)$ from $C_{av}(\tau)$ in

heating experiment (Figures S3A–S3L) at 24.5, 28.3, 29.6, 32.0, 35.6, 37.8, 41.9, 45.4, 51.9, 56.4, 60.2, and 64.9 °C. Maximum $J_{av}(v)$ at each temperature has J_{av}^{max} peak at 41.9 °C (Figure 5A). Similarly, Figures S1A–S1E show cooling from 64.6 to 25.3 °C at 0.2–0.3 K/min exhibited $I_f(t)$, $C(\tau)$, and $J(v)$. Figure 4B and Table S1B summarize Type I to V occurrences at each temperature. We computed $J_{av}(v)$ from $C_{av}(\tau)$, averaging twenty $C(\tau)$ waveforms (Figures S4A–S4L) at 64.6, 58.9, 54.3, 50.2, 46.2, 41.6, 37.7, 33.4, 31.5, 29.0, 26.6, and 25.3 °C. Maximum $J_{av}(v)$ at each temperature has J_{av}^{max} peak at 46.2 °C (Figure 5B).

The two peaks in Figures 5A and 5B (0.2–0.3 K/min) are separated by ≈4 K. This is likely due to hysteresis between heating and cooling. However, another pair of heating and cooling (1.0 K/min) experiments (Figures S8A and S8B) exhibited ≈9 K hysteresis at lower temperature. Thus, the heating and cooling experiments confirmed that $J_{av}(v)$ amplitude reached the top near T_g + 10 K, rather than the hysteresis from heating and cooling, that is, hysteresis
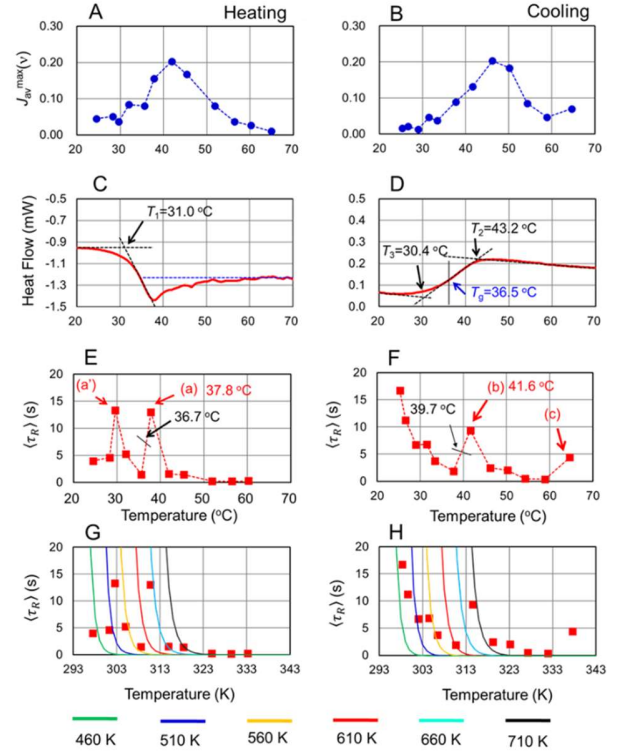
Figure 5. Temperature dependent maximum average power spectra, $J_{av}^{max}(v)$; DSC measurements; temperature dependent average relaxation time, $\langle \tau_R \rangle$; and $\langle \tau_R \rangle$ superposed with VFT lines: $J_{av}^{max}(v)$ for (**A**) heating (0.2 K /min) and (**B**) cooling (0.2–0.3 K /min); DSC traces for (**C**) heating and (**D**) cooling (5.0 K /min); $\langle \tau_R \rangle$ for (**E**) heating and (**F**) cooling; $\langle \tau_R \rangle$ for (**G**) heating and (**H**) cooling superposed with VFT lines (B= 460, 510, 560, 610, 660, and 710 K in green, blue, orange, light blue, and gray, respectively) computed from eq 4 using each B value. $J_{av}^{max}(v)$ is Fourier transform of $C_{av}(\tau)$, average twenty $C(\tau)$ traces, at each temperature. (**C**) and (**D**) show temperature zone switching from glass to melt and vice versa between $T_1 = 31.0 \approx T_2 = 30.4$ and $T_3 = 43.2$ °C including $T_g = 36.5$ °C. VFT lines for $B = 610, 660$, and 710 K were experimentally identified. [29]

6

behavior differed from experiment to experiment including different experimental conditions.

Figures 5C and 5D show PVAC DSC measurements for heating and cooling (5 K/min), respectively. We found three specific temperatures: T_1 = 31.0 °C (heating), T_2 = 43.2 °C (cooling), and T_3 = 30.4 °C (cooling). We found T_g = 36.5 °C (309.5 K) from the cooling experiment, that is, the midpoint of the gap between extrapolated glass and melt curves. We found PVAC T_g (297–315 K),[27] although no MW specifications were found. Generally, the higher the MW, the higher the T_g. From commercially available PVAC, we assume that MW ranges 90,000–600,000.[27] Thus, our T_g from MW 100,000 PVAC is within a reasonable range.

We found another temperature zone under the baseline (Figure 5C, broken blue line above T_1 = 31.0 °C), due to enthalpy overshoot,[13, 17] an endothermic process intrinsic to the heating procedure. These phenomena commonly occurred, and not only single dips (Figure 5C), but also multiple dips with various or fickle patterns for more than twenty DSC traces throughout the heating experiments; whereas, no enthalpy overshoots were observed for cooling experiments (Figure 5D).

Figures 5A–5D compare SMS and DSC observations considering two experimental conditions differences: surface and interface effects on T_g for polymer thin films, which generated different T_g from bulk polymer samples,[28] and heating and cooling rate differences (5.0 and 0.2–0.3 K/min for DSC and SMS, respectively). We used 4.0–8.0 mg PVAC powder as bulk PVAC for DSC, and a 300–400 nm thick PVAC film for SMS. Despite these experimental condition differences, a close relationship is reasonable between thermal properties evaluated by DSC and active collective motions occurrences for PVAC observed by SMS in the sense that $J_{av}(v)$ amplitude reached the top near T_g + 10 K, at which glass transition begin to start. This means T_g is likely close to glass transition temperatures probed by single-molecule Cy3 at interfaces T_g^{int} (see *Single Cy3 molecules sensing PVAC environment and specific temperatures above T_g* in *Discussion* for more detail).

Relaxation time evaluation from autocorrelation functions

This section explores the final major finding: discontinuous transition for temperature dependent $<\tau_R>$. Figures 5A and 5B show temperature dependent $J_{av}^{max}(v)$ for heating and cooling, respectively, to identify a temperature window where $C(\tau)$ cosine waveform preferentially occurred, typically in Figures 3C, 3D, S1B, and S1C for heating and cooling, respectively. However, $J_{av}^{max}(v)$ or originally $J(v)$ was insufficient to evaluate damped $C(\tau)$ oscillations, such as those in Figures 3F and S1F, because $J(v)$ extracted only oscillatory properties from $C(\tau)$ through frequency analysis. Thus, τ_R must also be considered to extract damping behavior from individual $C(\tau)$. Further motivation to evaluate τ_R and the reason for the use of eq 2, not product but summation of the two functions, are described in *Sub-second frequencies in power spectra and relaxation time evaluation* in *Discussion*. We evaluated τ_R from

$$C_{av}(\tau) = C_o \exp\left[-(t/C_1)^{C_2}\right] + C_3\cos(C_4 t + C_5) + C_6 , \quad (2)$$

where C_o, $C_1 = \tau_R$, $C_2 = \beta$, C_3, C_4, C_5, and C_6 are fitting parameters. The evaluated $C_1 = \tau_R$ is then converted into $<\tau_R>$.[9]

$$\left\langle \tau_R \right\rangle = \int_0^\infty e^{-(t/\tau_R)^\beta} dt = (\tau_R/\beta)\Gamma(1/\beta) , \quad (3)$$

where Γ is the gamma function, and the area under the KWW function in eq 3 denotes $<\tau_R>$; for exponential decay, β = 1 and $<\tau_R> = \tau_R$. The parameter β ranged 0.45 to 1.0 and 0.36 to 1.0 for heating and cooling, respectively (Figures S3 and S4). Evaluation of $<\tau_R>$ from $C_{av}(\tau)$ has substantial rationale based on GLE (see *Derivation of the $C(\tau)$ cosine waveform from generalized Langevin equation* in *Discussion*).

Figures 5A and 5E compare temperature dependent $J_{av}^{max}(v)$ and $<\tau_R>$ for heating experiments. Temperature at peak $J_{av}^{max}(v)$ is close to that at the peak above T_g (arrow (a)). Figures 5B and 5F show similar behavior for the cooling experiment. Peaks (a) and (b) at 37.8 and 41.6 °C, respectively, above T_g look abrupt and irregular changes. However, VFT lines superposed on Figures 5E and 5F provide another viewpoint in Figures 5G and 5H, respectively. We computed VFT lines from

$$\log(\omega_\infty/\omega) = B/(T - T_o), \quad (4)$$

where ω_∞ is the limiting angular velocity at infinite temperature, using B = 660 ± 50 K[29] in addition to other three B values, and then converted $\omega = 2\pi v$ into $<\tau_R>$ from $1/v = <\tau_R>$. Figures 5G and 5H suggest that something important occurs at 37.8 and 41.6 °C. For example, in the cooling experiment (Figure 5H) $<\tau_R>$ initially follows a VFT line (black, B = 710 K) and then suddenly alters its course within a zone restricted by VFT lines (green, blue, yellow, and red, B = 460, 510, 560, and 610 K, respectively). Two additional temperatures are marked in Figures 5E and 5F at 36.7 and 39.7 °C, being the midpoint between (a), (b) and their lowest temperature neighbor point as extrapolated temperatures, respectively. Further details about two pairs of temperatures 37.8 (36.7) °C and 41.6 (39.7) °C for heating and cooling, respectively are described in *Discontinuous transition of temperature-dependent relaxation times above T_g* and *Single Cy3 molecules sensing PVAC environment and specific temperatures above T_g* in *Discussion*.

DISCUSSION

We present arguments 1, 2, and 3 to help understand the major findings outlined in *Introduction* and explored in *Results*. Additionally, we also include a scheme to explain $I_f(t)$ fluctuation, Cy3 photophysics behind $I_f(t)$ fluctuation, and examining the validity of single Cy3 molecules sensing PVAC environment and glass transition in 4, 5, and 6, respectively.

1. Cosine waveform $C(\tau)$ derivation from GLE to provide the rationale behind observations in Figures 3C, 3D, S1B, and S1C, showing PVAC environment collective motion enclosing single-molecule Cy3.
2. Sub-second and second frequencies origin in $J(v)$ (Figures 3B–3D, 3F, S1B–S1D, and S1F) to provide

physical background and consistency between SMS and mechanical and dielectric spectroscopy observations.[29]

3. Temperature dependent $\langle\tau_R\rangle$ showing discontinuous transition (Figures 5E and 5F) similar to the cusp in second-order phase transition. This provides further evidence for second-order phase transition behavior in addition to *Point 1*.

4. Scheme for $I_f(t)$ fluctuation, substantiating the PVAC collective motion above T_g.

5. Cy3 photophysics to corroborate its viscosity sensitive fluorescence efficiency, supporting *Point 4*.

6. Cy3 sensitivity to PVAC surrounding viscosity and excitation polarization effect on fluorescence intensity.

Derivation of the $C(\tau)$ cosine waveform from generalized Langevin equation

The normalized autocorrelation function $C(\tau)$ is defined as

$$C(\tau) = R(\tau)/R(0), \tag{5}$$

where $R(\tau)$ is the autocorrelation function and $R(0)$ is a normalizing factor. $C(\tau)$ evaluation is a common method for characterizing specific temporal features from highly fluctuating experimental observations. We then evaluated $R(\tau)$ from $I_f(t)$

$$R(\tau) = \frac{1}{N}\sum_i^N I_f^o(i)I_f^o(i+\tau) \equiv \langle I_f^o(i)I_f^o(i+\tau)\rangle, \tag{6}$$

where $I_f^o(i) = I_f(i) - \bar{I}_f$; $\bar{I}_f$ is average $I_f(t)$ over 512 frames, $N = 256$ is the number of data points (half the number of the total frames) with step size or bin time $\Delta t = 36$ ms, i and τ are running suffix for each data point.

We summarize cosine autocorrelation function derivation[30] from the GLE[26]

$$\frac{dA(t)}{dt} = i\omega_o A(t) - \int_0^t \varphi(t-t')A(t')dt' + f(t), \tag{7}$$

where $A(t)$ is an any dynamical variable (generally a vector), ω_o is a formal angular frequency (generally a matrix with zero diagonal elements), $f(t)$ is a randomly fluctuating external force, and $\varphi(t - t')$ is a memory function combining $A(t)$ at t' (past) and t (present) given by

$$\varphi(t-t') = \frac{\langle f(t)f(t')\rangle}{\langle f(0)f(0)\rangle}. \tag{8}$$

Equation 8 is an essential result from GLE derivation,[26] signifying that the memory function is explicitly combined with normalized external force time correlation function. This equation is also a kind of fluctuation dispersion theorem. For the present derivation, $A(t)$ is a scaler variable equivalent to $I_f(t)$; hence $\omega_o = 0$ because it is a $[1 \times 1]$ dimensional matrix with zero diagonal.

GLE is applicable to Brownian motion analyses, and its use here is quite reasonable considering that polymer dynamics are modeled as polymer segment Brownian motion.[23] After several derivation steps from eq 7 (the skipped derivations are provided in *SI*),

$$\frac{d\Phi(t)}{dt} = -\omega^2 \int_0^t \varphi(t-t')\Phi(t')dt', \tag{9}$$

where ω^2 is constant and $\Phi(t)$ is a normalized autocorrelation function equivalent to $C(\tau)$,

$$\Phi(t) = \frac{\langle A(t)A(0)\rangle}{\langle A(0)A(0)\rangle}, \tag{10}$$

where $\langle A(t)A(0)\rangle$ is an autocorrelation function of $A(t)$. Substituting $\varphi(t - t') = 1$ into eq 9, that is, no memory function extinction approximation,[30]

$$\frac{d\Phi(t)}{dt} = -\omega^2 \int_0^t \Phi(t')dt' \tag{11}$$

and hence

$$\Phi(t) = \cos\omega t \tag{12}$$

because $\Phi(0) = 1$ from the normalized autocorrelation function definition. Thus, we have a cosine autocorrelation function with no memory function extinction approximation. This provides the rationale for $C(\tau)$ with remarkable cosine waveforms (Figures 3C and S1C) and can be explained as follows.

No memory function extinction means $\langle f(t)f(t')\rangle \approx \varphi(t - t') = $ constant, that is, $f(t)$ shows how PVAC collective motion coherently and persistently affects single Cy3 molecules as Brownian particles. On the other hand, instantaneous $\varphi(t - t')$ disappearance approximation provides a single exponential decay $C(\tau)$. Damped oscillation (Figures 3F and S1F) as intermediate waveforms between cosine and single exponential decay was dominantly observed. Figures S9A and S9B compare the two approximations for GLE.

Sub-second frequencies in power spectra and relaxation time evaluation

Frequencies lower than 1 Hz (0.109–0.542 Hz, Figures 3B–3D and 3F; and 0.217–0.868 Hz, Figures S1B–S1D and S1F) occurred for $J(v) > 0.05$. Thus, we investigated which factors determined these sub-second frequencies. From PVAC collective motion derived from $C(\tau)$ cosine waveforms, we expect that PVAC elasticity governs the collective motion. Polymer elastic properties, including PVAC, have widely been investigated using mechanical and dielectric spectroscopy.[29] One practical parameter to evaluate polymer elasticity is the shear modulus $G^*(\omega) = G'(\omega) + iG''(\omega)$, which can be mechanically evaluated by applying shear strain $\gamma = \gamma_o \sin\omega t$ to polymers under linear response condition.

Parameter $G''(\omega)$ represents shear modulus loss, that is, applied shear strain dissipated as heat, and exhibits maximum loss at ω_{max}, where shear strain efficiently excites dynamic polymer chain motion. Thus, ω_{max} with respect to T has been fitted to eq 4 and widely used for empirical α process analysis in polymer dynamics. Substituting experimentally derived $B = 450$ K, $T_o = 276$ K, and $\log\omega_\infty = 11.7$ at $T = 315$ K[29] into eq 4 produces a reasonable sub-second frequency: $\omega_{max} = 2\pi v = 1.452$ rad/s, or $v = 0.231$ Hz at $T = 42$ °C (315 K) (Figure S2A). This is consistent with experimental observations from Figures 3B–3D, 3F, S1A–S1D, and S1F, where prominent amplitudes were identified in $J(v)$ within 0.109–0.868 Hz. Figure S2B shows that frequencies indicated by dielectric loss $\varepsilon''(\omega)$ spectroscopy are also consistent with experimental observations, for example, $v = 0.133$ Hz at 315 K from eq 4 with $B = 610$ K, T_o

= 266 K, and log ω_∞ = 12.3. Thus, $J(\nu)$ identified specific sub-second frequencies ω in $C(\tau)$ being in reasonable agreement with those expected from eq 4 for ω_{max} observed by shear modulus loss $G''(\omega)$ and dielectric loss $\varepsilon''(\omega)$ spectroscopy.

From the above frequency evaluation, one may arouse a question that the analysis includes only one temperature (315 K) using eq 4, which comprehensively covers temperature dependent ω_{max}. This question is reasonable in the sense that temperature dependent frequencies should be analyzed from $J(\nu)$. As noted in Type I–V classification in *Temperature dependent single molecule fluorescence trajectories* in *Results*, initial intension faced toward temperature dependent frequency analysis in $J(\nu)$. We followed this direction if we always observed sharp and sufficiently isolated peaks in $J(\nu)$ at each temperature.

In fact, we observed peaks with substantial tailing (e.g., Figure 3F), and multiple peaks (e.g., Figures 3F, S1A and S1B) and those whose heights are close to background noises (e.g., Figure S1A), making systematic temperature dependent frequency analysis difficult. Also, 36 ms bin time and 256 frame temporal window (9.216 s, its reciprocal equals 0.109 Hz) limit frequency resolution. The number of frames and bin time were selected compromising with Cy3 photobleaching issue. Additionally, we employed a single exponential decay amplitude multiplied by one or more cosine function summation as a fitting function for $C(\tau)$. For example, a fitting function included four cosine function summation to obtain satisfactory fit in contrast to two dominant peaks, or frequencies in $J(\nu)$ (Figure 3F), whereas one cosine function for one prominent frequency in $J(\nu)$ generated insufficient fit (Figure S1F). These results suggest that fitting between $C(\tau)$ and calculated $C(\tau)$ are insufficient for frequency evaluation using only frequencies dominant in $J(\nu)$.

For these reasons, we decided to derive $\langle\tau_R\rangle$ from $C_{av}(\tau)$ at each temperature. Figures S3 and S4 present heating and cooling $C_{av}(\tau)$, respectively, showing wavy decay curves crossing base lines and commonly generating ν = 0.109 Hz in $J(\nu)$. This frequency is due to $C_{av}(\tau)$ curves crossing base lines one time in 256-frame time window. The frequencies higher than ν = 0.109 Hz mostly disappeared by averaging. Simplified $C_{av}(\tau)$ curves allow to include only one cosine function in eq 2. The use of $C_{av}(\tau)$ made it possible to evaluate $\langle\tau_R\rangle$ from $J_{av}(\nu)$ where it is impossible to extract frequency data (Figures S3L and S4J–S4L).

In Figures 3F and S1F, we used a product of one single exponential function and one cosine function or cosine function summation to treat $I_f(t)$ as a single damped oscillator in a conventional manner. In contrast, eq 2 is a summation of the KWW and cosine functions simply because the KWW and a cosine function product did not generate satisfactory fitting at all between $C_{av}(\tau)$ and calculated one. Based on simple probability calculation, the unsatisfactory fitting using two-function product is assumed to be the fact that "A and B" like the two-function product restricts the number of cases rather than "A or B" like two-function sum, where A and B represent the number of cases. Two-function product likely narrows

satisfactory fitting possibilities. The use of $C_{av}(\tau)$ not $C(\tau)$ probably causes such situation.

We abandoned analyzing temperature dependent frequencies directly from $J(\nu)$; instead, evaluated $\langle\tau_R\rangle$ from $C_{av}(\tau)$ curves. However, importance of Figures S2A and S2B is in explicitly pinpointing collective motion frequencies consistent with mechanical and dielectric spectroscopies.

Discontinuous transition of temperature-dependent relaxation times above T_g

We examine the significance for $\langle\tau_R\rangle$ at two temperature pairs 37.8 (36. 7) °C and 41.6 (39.7) °C in Figures 5E and 5F. These temperatures fall within the zone (30.4–43.2 °C) considered in *Specific temperature window above T_g* in *Results*, where $J_{av}^{max}(\nu)$ is enhanced (Figures 5A and 5B). Higher $J_{av}^{max}(\nu)$ amplitude tended to be associated with enhanced $C_{av}(\tau)$ cosine characteristics (Figures S3A–S3L and S4A–S4L), although not exclusively (Figures S3E, S3F, S4F, and S4G). We thus consider two temperature pairs 37.8 (36. 7) °C and 41.6 (39.7) °C to be T_c and T_c' for heating and cooling, respectively through the following discussion. The temperatures in parentheses in each pair are simply due to difference in viewpoint about the $\langle\tau_R\rangle$ data in Figures 5E and 5F.

Perfect cosine $C(\tau)$ without damping shows infinite τ_R in a similar way that order parameters, for example C_p, in second-order phase transition diverge at T_c

$$C_p \propto \varepsilon^{-\alpha}, \tag{13}$$

where $\varepsilon = (T - T_c)/T_c$ and α is a critical-point exponent.[19] Experimental order parameters show prominent peaks called cusp in discontinuous transition.[18, 19] Similarly, $\langle\tau_R\rangle$ exhibits prominent peaks at T_c = 37.8 and T_c' = 41.6 °C similar to order parameter discontinuity. One may argue against this similarity statement compared with typical second-order phase transition in liquid helium C_p characterized by λ-shape transition in cusp-shape discontinuity.[18, 19] Considering average $\langle\tau_R\rangle$ characteristic, however, $C(\tau)$ diversity before averaging (Figures 4A and 4B; Tables S1A and S1B), and the limited number of data points in Figures 5E and 5F, the similarity is acceptable. The issue of the limited data points is noted in the end of this section. These different T_c and T_c' on heating and cooling just reflect that the present discontinuous transitions are not real second-order phase transition indications. Thus, based on the above consideration validity, second-order phase transition behavior was observed not only in cosine $C(\tau)$ but also in temperature dependent $\langle\tau_R\rangle$.

Figures 5G and 5H superpose temperature dependent $\langle\tau_R\rangle$ in Figures 5E and 5F on VFT lines, providing another viewpoint for second-order phase transition behavior, that is, T_c = 36.7 and T_c' = 39.7 °C, respectively. In Figures 5G and 5H, data points at 37.8 and 41.6 °C form the edges of discontinuous connection from one VFT line to another or to a zone formed by several VFT lines. For heating, $\langle\tau_R\rangle$ follows a VFT line determined by B = 560 K from 302.6 K (29.6 °C, arrow (a')), and then tracks another VFT line determined by B = 660 K. For cooling, $\langle\tau_R\rangle$ first follows the black VFT line determined by B = 710 K from 331.9 K (58.9 °C), and then cross VFT lines determined by

B = 610, 560, and 510 K. The appearance of the edge is similar to a cusp in the temperature dependent order parameter for second-order phase transition. Thus, we consider 36.7 and 39.7 °C extrapolated to each midpoint to be T_c and T_c' for heating and for cooling, respectively.

There were two irregularities regarding <τ_R>: an additional peak occurred below 30 °C for heating (Figure 5E, arrow (a')) and the point indicated at 64.6 °C for cooling (Figure 5F, arrow (c)). The first irregularity is against the expectation that <τ_R> increases with decreasing temperature below T_g due to increased PVAC viscosity. This irregularity may be associated with fickle endothermic enthalpy overshoots for heating DSC measurements. As noted in *Specific temperature window above T_g* in *Results*, enthalpy overshoot observations varied from experiment to experiment below T_g = 36.5 °C. Although DSC measurement differs from SMS, we assume that reduced <τ_R> at the two points below 30 °C (Figure 5E) is due to fickle endothermic overshoots reducing PVAC viscosity. Another heating experiment (Figures S8C and S8E) likely supports the assumption, where <τ_R> increases smoothly with decreasing temperature below 40 °C. This may be due to free from endothermic overshoot disturbance, or simply due to temperature intervals in Figures S8C and S8E (≈ 10 K interval) being broader than those in Figures 5E and 5G (≈ 3 K interval), practically missing enthalpy overshoots. The second irregularity is characterized by <τ_R> larger than expectation at 64.6 °C in Figure 5F. This is reflected by decreased $C(\tau)$ in Type V, as shown in Figures 4A and 4B. This irregularity did not occur for another cooling experiment (Figure S8D).

Aside from these irregularities, we commonly observed that <τ_R> increased with decreasing temperature for both heating and cooling, with specific temperatures T_c = 37.8 (36.7 °C) and T_c' = 41.6 (39.7 °C), respectively above T_g. These are essential observations in temperature dependent <τ_R>. Increasing <τ_R> with decreasing temperature below T_g = 36.5 °C is reasonable considering increased viscosity at lower temperatures and Cy 3 viscosity-sensitive nature.

One may feel that the number of <τ_R> data points in Figures 5E–5H is totally insufficient to consider the discontinuous change as a cusp-shape transition by comparing the figures with widely-known λ transition in liquid helium C_p where several tens data points were included at m K to 10 μK intervals.[19] However, photobleaching issue in SMS limited the number of <τ_R> data points, as stated in *Observation of single Cy3 molecules* in *Results* and noted in *Conclusions*.

Proposed scheme for intermittent single-molecule Cy3 fluorescence trajectories

We constructed a scheme to understand temperature dependent $I_f(t)$, especially showing intermittent fluctuations at T_g + 10–20 K (Figures 3C–3F, S1A–S1C, and S2F), based on three facts.

1. Cosine waveforms in $C(\tau)$, signifying collective motion for PVAC enclosing single-molecule Cy3 probes.
2. Photophysics for viscosity sensitive Cy3 fluorescence efficiency.

3. Resonance frequencies in PVAC viscoelasticity and dielectric properties consistent with sub-second frequencies in $J(\nu)$.

The scheme incorporates assumed tube-like PVAC structures (Figure 6A) enclosing a Cy3 molecule and signifying collective motion. Fluorescence intensity is modulated by collective tubular PVAC chain expansion and contraction (Figures 6B and 6C, respectively) in the sub-second regime. The expanded tube makes torsional motion active in Cy3, enhancing viscosity-sensitive non-radiative pathways to quench fluorescence, whereas the contracted tube restricts torsional motion to confine non-radiative pathways. PVAC viscoelasticity is supposed to control collective contraction and expansion frequencies. We describe these non-radiative pathways in the subsequence section.

The proposed scheme can be associated with a possible size for the assumed tube-like structure with ξ_α = 2–4 nm for PVAC,[31, 32] which reasonably approximates the tube-like structure size enclosing Cy3 smaller than 1 nm.

Cy3 photophysics behind intermittent single-molecule Cy3 fluorescence trajectories

Our approach to identify polymer dynamics near T_g depends on the requirement that Cy3 fluorescence probes surrounding viscosity fluctuations through $I_f(t)$. Cy3 photophysics explains $I_f(t)$ changes, and has been reported,[33, 34] providing a feasible scenario for viscosity sensitive fluorescence efficiency. After outlining Cy3 fluorescence viscosity sensitivity, we describe non-radiative pathways fundamentals for Cy3 photophysics, and review previous reports supporting sub-second off-times. Finally, we present a scenario for the temperature dependent off-times in $I_f(t)$.

Twisting motion around the polymethine chain connecting two heterocycles (Figure 6D) controls non-radiative transition from the lowest excited singlet state S_1 (fluorescent state) to the twisted lowest excited singlet state S_1^{tw} (non-fluorescent state). This transition opens the gateway to non-fluorescent dark states, such as twisted lowest triplet state T_1^{tw} followed by twisted ground state S_0^{tw}. Highly viscous media, such as glycerol and polymers, restrict non-radiative transition $S_1 \rightarrow S_1^{tw}$, hence enhance fluorescence efficiency.

Non-radiative pathways in Cy3 to understand the origin for off-times in $I_f(t)$ are characterized by twisted molecular structures with torsional angle θ modeled at 90 ° (Figure 6D). The S_1^{tw} energy level approaches that for T_1^{tw} and S_0^{tw},[33, 34] enhancing non-radiative intersystem crossing (ISC) $S_1^{tw} \rightarrow T_1^{tw}$ (rate constant k_{ST}).[33] This pathway is followed by ISC $T_1^{tw} \rightarrow S_0^{tw}$ (rate constant k_{TS}). Enhanced non-radiative pathways in the twisted molecular structure are based on the energy gap law for non-radiative transitions,[35] where smaller energy gap between two energy levels produces faster non-radiative transitions. Thus, the key consensus among early studies was that conformational isomer S_1^{tw} formed the gateway to non-radiative Cy3 pathways.

Longer off-times, 0.1–1.0 s, in highly fluctuating $I_f(t)$ (Figures 3C, 3D, 3F, S1B, S1C, and S1F) can be best understandable by reference to a previous publication. Hofkens and De Schryver et al.[33] reported intermittent fluorescence (i.e., on and off) from single-molecule cyanine dyes, not including Cy3, with polymer overlay at room temperature. They concluded that the lowest triplet state T_1 comprises a dark state, which accounts for the off-times and
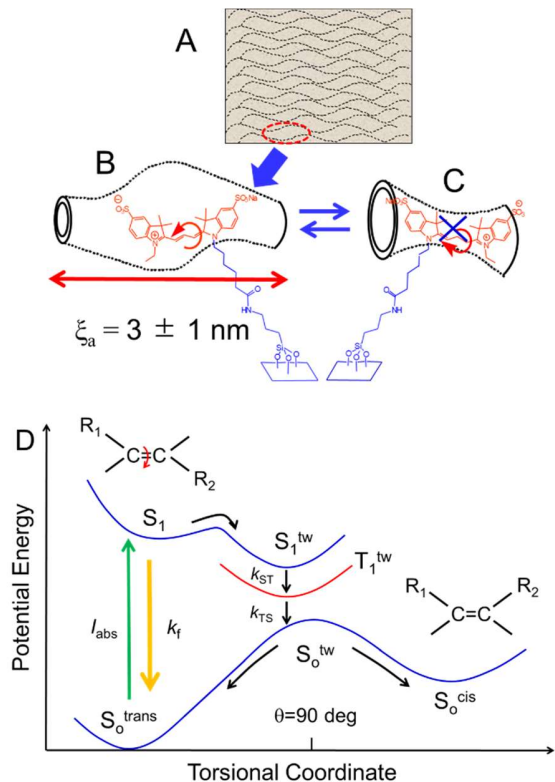
Figure 6. Proposed collective motion scheme for PVAC enclosing single-molecule Cy3 and photophysical processes in Cy3 to consider sub-second off-times in $I_f(t)$. (**A**) Assumed tube-like PVAC structure signifying collective motion; (**B**) expanded tube allowing torsional motion for Cy3 active, enhancing viscosity-sensitive non-radiative pathways, and quenching fluorescence to generate off-times in $I_f(t)$; (**C**) contracted tube restricting torsional motion, prohibiting non-radiative pathways that quench fluorescence, recovering fluorescence emission; (**D**) continuous 532-nm excitation (I_{abs}) allows continuous $I_f(t)$ from S_1 when non-radiative pathways generating off-times much longer than 36 ms are not dominant. In contrast, dominant non-radiative pathways involving bulky torsional motion around the polymethine bond ($S_1 \rightarrow S_1^{tw} \rightarrow T_1^{tw} \rightarrow S_o^{tw} \rightarrow S_o^{trans}$ or $S_1 \rightarrow S_1^{tw} \rightarrow T_1^{tw} \rightarrow S_o^{tw} \rightarrow S_o^{cis} \rightarrow S_o^{tw} \rightarrow S_o^{trans}$) interrupt fluorescence emission to generate 0.1–1.0 s off-times. Time-resolution 36 ms smears off-times much shorter than 36 ms, hence off-times 0.1–1.0 s is detectable when highly viscosity dependent transition $S_o^{cis} \rightarrow S_o^{tw} \rightarrow S_o^{trans}$ becomes a rate determining step. PVAC viscoelasticity likely decides sub-second contraction and expansion frequencies for the tube-like structure. In (**B**), the tube-like structure size is assumed to be equivalent to that of PVAC CRR, $\xi_a = 3 \pm 1$ nm. [31]

proposed that chromophore torsional motion is involved in the off-times. They also reported average $k_{TS} = 35$ and 39 s^{-1} (0.029 and 0.026 s, respectively) for cyanine dyes not including heavy atoms (e.g., Se), which enhance non-radiative k_{TS} due to heavy atom effects.[35]

These average times faster than 0.1 s were measured by time resolution 0.5–1.0 ms ranges,[33] which is much

faster than 36 ms used in the present article. However, these results do not contradict the observed 0.1–1.0 s off-times because the previous study includes substantial data smaller than $k_{TS} = 10$ s^{-1} before averaging; whereas, SMS used in the present study smeared fluctuations much faster than 36 ms time resolution. The previous study focused on ISC characterized by events much faster than 1.0 s. Comparing earlier conclusions and proposals[33, 34] with the current findings in $I_f(t)$ regarding photophysical pathways (Figure 6D), we consider the possibility that $S_o^{cis} \rightarrow S_o^{trans}$, or *cis* → *trans* isomerization rate rather than ISC (rate constant k_{TS}), controls the off-times. Generally, *cis* → *trans* isomerization rate strongly depends on surrounding viscosity due to its bulk. We found *cis* → *trans* isomerization rate in the polymer matrix to be consistent with off-times 0.1–1.0 s. Grebenkin and Bol'shakov[36] reported rate constants for *cis* → *trans* isomerization from three azo compound types doped in a poly(methyl methacrylate) matrix at room temperatures in the dark after light-driven *trans* → *cis* isomerization. One of the azo compounds (1,1'-azonaphthalene) has size close to Cy3, and exhibited rate constants $k_1 = 0.16$ min^{-1} and $k_2 = 0.012$ min^{-1} (hence $1/k_1 = 0.104$ s and $1/k_2 = 1.389$ s), derived by bi-exponential fitting the observed kinetics at 287 K. Thus, the off-times 0.1–1.0 s in $I_f(t)$ we observed are not absurd in spite of differences between azo compound and Cy3, considering that a rigid matrix significantly hinders torsional motion and hence would become a rate determining hindrance in *cis* → *trans* isomerization.

Here, we can qualitatively explain temperature dependent off-times in $I_f(t)$ for heating (Figures 3C–3F) and cooling (Figures S1A–S1C and S1F) as follows. Off-times is exclusively determined by the non-radiative pathways $S_1^{tw} \rightarrow T_1^{tw} \rightarrow S_o^{tw} \rightarrow S_o^{trans}$ or $S_1^{tw} \rightarrow T_1^{tw} \rightarrow S_o^{tw} \rightarrow S_o^{cis} \rightarrow S_o^{trans}$ (Figure 6D). Figure 3A shows $I_f(t)$ without off-times at 24.5 °C, that is, off-times much faster than 36 ms are invisible in $I_f(t)$ measurement. Once S_o^{cis} is substantially populated, off-times governed by transition $S_o^{cis} \rightarrow S_o^{trans}$ become visible even for 36 ms frame rate at temperatures > 24.5 °C. Thus, $I_f(t)$ exhibits 0.1–1.0 s off-times at 41.9 °C (Figure 3C). Further increasing temperature enhances $S_o^{cis} \rightarrow S_o^{trans}$, $S_1 \rightarrow S_1^{tw}$ after photoexcitation, and rate determining $S_o^{cis} \rightarrow S_o^{trans}$, giving $I_f(t)$ off-times much shorter than 1.0 s for temperatures > 60 °C (Figures 3E and S1A).

Single Cy3 molecules sensing PVAC environment and specific temperatures above T_g

We utilized single Cy3 molecules covalently immobilized on a quartz surface with PVAC overlay. One possible concern is that such interface-confined sample may fail to detect changes in PVAC thermal properties due to interface effects. To address this concern, we must use a bulk sample in a surface and interface free manner. Although SMS could not be implemented for such a sample, we limited our attention only to consider interface effects due to the surface immobilized sample free from surface effects. We thus compared SMS observations with and without PVAC overlay.

Here, we describe observations 1, 2, and 3 confirming that Cy3 feels the PVAC environment. The first one is

11

noted in *Observation of single Cy3 molecules*, the second and the last ones are noticed in *Major findings and others, overview* in *Results*. Additionally, we have observation 4 that Cy3 molecules with PVAC overlay prefer horizontally polarized excitation to absorb excitation light and emit fluorescence as much as possible. Change in absorption transition moments during SMS measurement is negligible.[37] Thus, intrinsic inhomogeneity in polymer structures and change in local viscosity dominate $I_f(t)$ fluctuations.

1. Photobleaching was reduced from 35–40% without PVAC overlay to 17–23% with PVAC overlay, confirming that the PVAC overlay protects Cy3 from photobleaching participation by oxygen.[33]
2. Figures S5A and S5B show average fluorescence intensity enhancement (2.16-fold) with PVAC overlay.
3. Figures S6A–S6C show that $C(\tau)$ waveforms without PVAC overlay exhibited single exponential decay at 22.1 °C with $\tau_R = 0.05$–0.14 s. We selected highly fluctuating $I_f(t)$, comparable to those in Figures 3D, 3E, and S1B to contrast no observed cosine waveform $C(\tau)$ without PVAC overlay and cosine waveform $C(\tau)$ with PVAC overlay.
4. Figures S7A–S7D show excitation polarization effects on observed fluorescence intensity, confirming that horizontally polarized excitation is advantageous to provide more fluorescence photons (1.77- and 1.50-fold at 24.0 and 56.3 °C, respectively), ruling out the possibility that Cy3 molecules enclosed by PVAC considerably rotate on the surface even at the elevated temperature.[37]

Thus, we have substantial evidence that single-molecule Cy3 really feels the PVAC overlay. Additionally, there was also experimental evidence that fluorescence quantum efficiency Φ_f for Cy3 increased with increasing solvent viscosity.[25] Hence, florescence intensity variations in $I_f(t)$ also depend on local PVAC viscosity. The viscosity dependence of fluorescence intensity is the most important requirement for Cy3 use as a viscosity sensitive single-molecule probe.[7]

However, glass transition detection by SMS using surface immobilized Cy3 raises further issues.

1. Cy3 detection of glass transition related temperatures for glass-forming materials irrespective of surface, interface, or bulk.
2. Relationship between PVAC T_g and T_g^{int}.

Before considering the first issue, recall criteria for glass transition: $\eta \approx 10^{12}$ Pas and $\tau_R \approx 100$ s noted in *Introduction*. One may feel it is impossible to detect T_g with Cy3 or more generally viscosity-sensitive dye fluorescence considering the criteria; however, it is possible. Malachite green (MG), a widely-known viscosity-sensitive triphenyl methane dye, probed T_g for several alcohols and a polymer without side chains, with $T_g = 100$–200 K. Moreover, MG identified another crossover temperature below T_g near 200 K for polymers with side chains, including PVAC. These outcomes were produced from picosecond time-resolved fluorescence spectroscopy using bulk MG in alcohols or doped in polymer thin films.[6, 14, 15] These achievements do not mean that picosecond time resolution detected $\tau_R \approx 100$ s but identified crossover temperatures through temperature dependent MG fluorescence lifetimes 100–1000 ps. Thus, viscosity sensitive dyes identify T_g for many glass forming materials in bulk, such as alcohols and polymers.

The following consideration probably settles the second issue. Our basic idea is that T_g evaluated by DSC is likely close to glass transition temperatures at interfaces T_g^{int}, as noted in *Specific temperature window* above T_g in *Results*. In other words, PVAC thermal properties at interface are close to bulk PVAC in the present study. This idea is supported by the fact that PVAC T_g^{int} depends on PVAC mobility adsorbed on silica.[38] The mobility is classified into mobile (surface), loosely bound (bulk), and tightly bound (interface). Glass transition temperatures increase decreasing PVAC mobility and increasing MW, ≈ 20–35, ≈ 35–58, and ≈ 58–70 °C for mobile, loosely-bound, and tightly-bound PVAC, respectively, for PVAC (MW 260, 000).[38]

As for our experimental observations, the interaction between 300–400 nm thick PVAC (MW 100, 000) film and quartz surface can be loosely-bound PVAc in the above classification because the quartz surfaces we prepared were hydrophobic due to surface silanization (see *Sample preparations* in *Materials and Methods*), whereas PVAC is hydrophilic. Thus, considering that the PVAC thermal properties probed by surface immobilized single Cy3 molecules on silanized quartz surface present those of tightly bound PVAC is totally unrealistic. The PVAC MW we used in the present study (MW 100,000) was smaller than that (MW 280,000) used.[38] Thus, we preferably consider possible PVAC T_g^{int} to be a lower boundary in ≈ 35–58 °C, which includes not only $T_g = 36.5$ °C but also $T_c = 37.8$ (36.7) °C and $T_c' = 41.6$ (39.7) °C (Figures 5E and 5F).

Both T_c and T_c' are included within the 30–43 °C zone evaluated by the DSC (Figures 5C and 5D) and the loosely-bound ≈ 35–58 °C zone. Can both T_c and T_c' be T_g^{int}? Here, we remember that the specific temperature in the VFT equation is the Vogel temperature T_o and not T_g. Thus, T_c and T_c' specifically appeared along VFT lines cannot be PVAC T_g^{int}. Assuming that $T_g \approx T_g^{int}$, both T_c and T_c' are just the temperatures at which cusp-shaped $<\tau_R>$ discontinuity was observed, characterizing second-order phase transition in glass transition.

Figures S8E and S8F confirm that $<\tau_R>$=101 s at 20.7 and 24.4 °C for heating and cooling, respectively. Simply following the glass transition criterion $\tau_R \approx 100$ s leads to $T_g = 20.7$–24.4 °C, which can be glass transition temperatures for mobile PVAc.[38] However, the idea that PVAC probed by SMS using surface-immobilized single molecules is classified into mobile is unrealistic. Thus, $\tau_R \approx 100$ s criterion is only a rule of thumb for glass transition. The $<\tau_R> = 101.2$ s is evaluated by a limited time window 9.22 s (256 frame) in SMS to evaluate $C(\tau)$. One may suspect that such a small time-window detects much larger $<\tau_R>$. This is because Γ function in eq 3 contributes more than 100 s to $<\tau_R>$ for $\beta \leq 0.5$. For example, Figure S8E shows

that combining $1/\beta$ and $\Gamma(1/\beta)$ converts $\tau_R = 39.5$ s at 20.7 °C to $\langle\tau_R\rangle = 101.2$ s.

CONCLUSIONS

We identified two sets evidence for second-order phase transition behavior in PVAC glass transition within a specific temperature window between 30 and 60 °C, or more exclusively between T_2 and T_3 (Figure 5D) including $T_g = 36.5$ °C and below $T_{cross} \approx 1.2T_g = 98.4$ °C, verifying the original classification of glass transition as the pseudo-second order transition.[16]

1. Highly active PVAC collective motions from $C(\tau)$ cosine waveforms above T_g,
2. Cusp-shape discontinuous transition in temperature dependent $\langle\tau_R\rangle$.

Second-order phase transition behavior in glass transition has been suggested in temperature dependent S, C_p, and η as noted in *Introduction*. These parameters temperature dependence is solid experimental facts. However, such knowledge has lacked straightforward evidence for critical phenomena in glass transition mainly due to experimental limitations. The achievements in the present article have disclosed critical phenomena in glass transition based on molecular-level experimental observations and make a breakthrough in deeply understanding glass transition from theoretical point of view[21] to settle a major unresolved problem in physics and chemistry.[12, 13]

The essential findings, *Point 1 and 2*, arose from SMS, which is an unconventional method for glass transition investigation in contrast to the more widely used DSC, dielectric and mechanical spectroscopy, and so on. However, SMS in the present our status has one inability and two technical limitations in return for the uniqueness demonstrated in the present article.

• No direct ξ_α evaluation but no critical opalescence observation from PVAC, suggesting $\xi_\alpha < 100$–200 nm.
• Photobleaching in Cy3, or any viscosity-sensitive fluorescent dyes. This issue prevents repeated video imaging, which limits the number of data points in Figures 5G and 5H. Photobleaching mainly occurs due to photochemical reactions involving oxygen by way of T_1, or specifically T_1^{tw} for Cy3 (Figure 6D). Thus, in principle photobleaching can be avoided by removing oxygen from the sample.
• Limited temperature range. We used a hot plate to raise the samples from room temperature (20–25 °C) to 90 °C. Although this is not an issue for PVAC, this limits polymer selection to those with $T_g = 30$–70 °C.

We have now a commercial temperature controller –190–600 °C for microscope use (https://www.jht.co.jp/). To apply this system to SMS we must optimize mechanical conflict between the temperature controller and SMS optical setup. Extending temperature range would facilitate opportunities to handle various industrially important polymers for SMS evaluation near T_g.

MATERIALS AND METHODS

Experimental design

We used single-molecule samples and video microscopy for SMS measurements including a light microscope, video camera, and CW laser; in addition, a DSC device to evaluate PVAC T_g. Although it was reported in many literatures, we evaluated again and again T_g to check reproducibility especially in heating experiments. In SMS, a conventional video microscopy setup was adequate, but not up to recent developments. Hence, practical expertise with considerable care was required to prepare good SMS samples with low background and many randomly and uniformly distributed single molecules within the microscope field of view (Figure 2B). Selecting laser power and image intensifier gain was a particular area based on our previous expertise because excessive intensifier gain enhancement uselessly increased background noise. The reasons for covalently immobilized single-molecule Cy3 use were described in elsewhere.[7]

Sample preparations

The basic strategy to prepare surface immobilized single Cy3 molecules (Figure 2A, inset) is Cy3-NHS ester conjugation to form a covalent bond with an amino group through its NHS ester group. The amino group should be included in a silane coupling chemical, covalently bounded in advance with hydroxyl groups intrinsic to the quartz surface. The procedures included four steps as follows.

1. Synthetic quartz plates (ES grade, 30 × 30 × 1.0 mm, Fujiston, Osaka) rich in hydroxyl groups were selected as substrates to ensure as much silanization as possible while retaining minimal optical background. The supplied quartz plates were cleaned by immersing them in 50 : 50 (v/v) HCl (6 M) and 5.0% NaClO solution for 2–3 h or longer until Cl_2 gas was substantially exhausted, rinsed with deionized water, and then blown dry using nitrogen jet. To reuse quartz plates after SMS measurement, emersion oil on the surface was thoroughly wiped off using a grease removing spray for industrial use (https://www.cainz.com/jp), the PVAC layer was removed with acetone, and the quartz plate was washed with 50 : 50 w/w KOH/deionized water to recover hydrophilic quartz surfaces by removing the silane coupling chemical on the surfaces.
2. We used 3-aminopropyltriethoxy silane (3-APTES, nacalai tesque 02309–62, Kyoto) to prepare amino groups on prepared quartz plates from step (1). The plates were sonicated in acetone (99.5 % Wako 012–00343, Tokyo) solution (1% v/v) with 3-APTES for 30 min at 23 °C. Excess silane solution on the surface was washed away by pouring acetone (99% Wako 01100357, Tokyo) over the surfaces three to five times, and the washed surface was dried using nitrogen jet.
3. We dissolved Cy3-NHS ester (1 mg, Amersham GE Healthcare 9713899, UK) in DMSO (99% Wako 049–07213, Tokyo) to avoid possible dye aggregation, and then successively diluted into 0.0415 mM solution with (50 : 50 v/v) ethylene glycol (99.5% Wako 058–

00986) /deionized water to prepare a Cy3-NHS ester solution for frozen storage.

Cy3-NHS stock solution was diluted to 5–20 pM with deionized water to prepare isolated single Cy3 molecules on a quartz surface (Figure 2B). Two to three drops of diluted Cy3-NHS solution were put on a functionalized quartz surface, and then kept in a shaded box for 30 min at room temperature (20–25 °C). Prepared quartz surfaces from step (2) become hydrophobic rather than hydrophilic through functionalization by 3-APTES, indicating successful surface silanization. Thus, the Cy3-NHS solution formed a swollen mass on the hydrophobic surface. After incubation, excess Cy3-NHS solution was pipetted away, the surface was washed by pouring deionized water three to five times, and then dried using nitrogen jet.

4. Cy3 molecules covalently bound on the surface were covered with a thin film of PVAC (average MW ≈ 100,000, Sigma–Aldrich 189480–25G, Tokyo) by spin casting PVAC (5% w/w) in ethyl acetate (Wako 99.5% 051–00356, Tokyo) at 2500 rpm. The PVAC covered surface was nitrogen purged to avoid undesirable humidity causing foggy surface. Prepared samples were incubated in a drying chamber at least 1 h at 100 °C, that is, much higher than PVAC calorimetric glass transition temperature T_g = 36.5 °C (Figure 5D), and then placed overnight in a vacuum chamber (5 kPa). PVAC film thickness was ≈ 400 nm when 5% w/w PVAC solution was used, measured using a stylus surface profiler (Alpha–Step IQ, KLA–Tencor, CA, USA).

Instruments used for SMS

Fluorescence video images were captured with an upright microscope (Optiphot, Nikon, Tokyo) for metallurgical use equipped with an objective lens (×100, NA 0.85, GLF–PLACH100XLM, Wraymer, Osaka) and optical filter designed for Cy3 fluorescence (ET610/75m, Chroma, USA). This type of microscope allowed to use an air-gapped objective lens (Figure 2A) free from coverslip, immersion fluid between the coverslip and objective lens, and optical contact between coverslip and sample surface, which were convenient SMS to avoid thermal disturbance to the objective lens.

We used a CCD camera (C4880–80, Hamamatsu Photonics, Japan) and image intensifier (C8600–3, Hamamatsu Photonics, Japan) to obtain single-molecule sensitivity at 36 ms/frame. Video images were processed with HC Image Live U1158–08, Hamamatsu Photonics, Japan and Image–Pro Premier 9.3, Media Cybernetics, MD, USA. Evaluation of $C(\tau)$ and Fourier transform of $C(\tau)$ to obtain $J(v)$ was carried out in Excel 2013. Evaluation of τ_R was processed with Igor Pro version 6 (WaveMetrix, OR, USA).

Horizontally polarized CW laser beam (532 nm, MGL–FN–532nm–1W, Sunplus Tokyo) was used to excite Cy3 samples in prism-based evanescent illumination configuration (Figure 2A). We placed a half-wave (Sunplus Tokyo) or quarter wave (Sunplus Tokyo) plate after the CW laser outlet to control the laser output polarization. Frame rate (36 ms/frame), number of frames (512), and laser power density (16 W/cm²) were selected to compro-

mise among sufficient fluorescence intensity, acquiring sufficient frames, and reducing Cy3 molecule photobleaching.

Thermal analysis and sample temperature control

Glass transition and other PVAC specific temperatures were evaluated using a differential scanning calorimeter (Thermo Plus EVO DSC 8230, Rigaku, Tokyo) from –7 to 100 °C and 100 to –7 °C at 5 K/min in a flowing nitrogen atmosphere with 60 min-interval between heating and cooling. PVAC mass was 5.0–10.0 mg, typically 7.0–8.0 mg, and equivalent Al_2O_3 powder mass was used as a reference.

Sample surface temperatures in SMS were controllable from room temperature (20–25 °C) to above 80 °C using a hot plate for microscope use (Thermo Plate TP–S–100, Tokai Hit, Shizuoka, Japan) and monitored with an infrared thermometer (IT–545S, Horiba, Kyoto).

When heating a sample under the microscope, we used 24.5 (starting at room temperature), 28.3 (27.0), 29.6 (30.0), 32.0 (33.0), 35.6 (35.0), 37.8 (40.0), 41.9 (45.0), 45.4 (50.0), 51.9 (55.0), 56.4 (60.0), 60.2 (65.0), and 64.9 (70.0) °C. Temperatures were monitored at approximately 15 min intervals from 24.5 to 35.6 °C (0.19 K /min) and approximately 20 min intervals from 35.6 to 64.9 °C (0.21 K /min). The numbers in parentheses denote temperatures adjusted by the hot plate controller.

For cooling a sample under the microscope we observed 64.6 (70.0), 58.9 (65.0), 54.3 (60.0), 50.2 (55.0), 46.2 (50.0), 41.6 (45.0), 37.7 (40.0), 33.4(35.0), 31.5 (33.0), 29.0 (30.0), 26.6 (27.0), and 25.3 °C (finishing at room temperature) on the sample surface. Temperatures were monitored at approximately 15 min intervals at 64.6–41.6 °C (0.31 K /min) and approximately 13 min intervals at 41.6–25.3 °C (0.21 K /min).

Samples were exposed in the air, causing the difference between adjusted and observed temperatures. Before starting the cooling experiment, samples were heated from room temperature to 64.6 °C, over approximately 90 min (0.45 K/min), and annealed at the final temperature (64.6 °C) for 60 min before reducing the temperature to 25.3 °C.

Independent samples were used for the heating and cooling experiments (Figures 3–5, S1, S3, and S4) to minimize Cy3 photobleaching, particularly given the limited number of fluorescent spots in the field of view. On the other hand, the same sample was used in Figure S8 because the sample was an ideal one characterized by the uniformly distributed a sufficient number of single Cy3 molecules free from photobleaching even after changing widely the view field.

ASSOCIATED CONTENT

Corresponding Author

*E-mail: mi195526@josai.ac.jp

ORCID

Mitsuru Ishikawa: 0000-0001-9438-2270
Takayuki Uwada: 0000-0002-4272-7964

REFERENCES AND NOTES

1. Single molecule spectroscopy, Nobel conference lectures, Eds. R. Rigler, M. Oritt, T. Basché, Springer 2001.
2. L. Kisley, C. F. Landes, Molecular approaches to chromatography using single molecule spectroscopy. *Anal. Chem.* **87**, 83–98 (2015).
3. S. Ray, J. R. Widom, N. G. Walter, Life under the microscope: single-molecule fluorescence highlights the RNA world. *Chem. Rev*. **118**, 4120–4155 (2018).
4. J. C. Scaiano, A. E. Lanterna, Is single-molecule fluorescence spectroscopy ready to join the organic chemistry toolkit? A test case involving click chemistry. *J. Org. Chem.* **82**, 5011–5019 (2017).
5. T. Tachikawa, S. Yamashita, T. Majima, Evidence for crystal-face-dependent TiO_2 photocatalysis from single-molecule imaging and kinetic analysis. *J. Am. Chem. Soc.* **133**, 7197–7204 (2011).
6. M. Ishikawa, J. Y. Ye, Y. Maruyama, H. Nakatsuka, Triphenylmethane dyes revealing heterogeneity of their nanoenvironment: femtosecond, picosecond, and single-molecule studies. *J. Phys. Chem. A* **103**, 4319–4331 (1999).
7. V. P. Biju, J. Y. Ye, M. Ishikawa, Spatial heterogeneity in a polymer thin films probed by single molecules. *J. Phys. Chem. B* **107**, 10729–10735 (2003).
8. N. Adhikari, N. A. Capurso, D. Bingermann, Heterogeneous dynamics and dynamic heterogeneities at the glass transition probed with single molecule spectroscopy. *J. Chem. Phys.* **127**, 114508 (2007).
9. T. Oba, M. Vach, Relaxation in thin films mapped across the film thickness by astigmatic single-molecule imaging. *ACS Macro Lett.* **1**, 784–788 (2012).
10. M. F. Serag, M. Abadi, S. Habuchi, Single-molecule diffusion and conformational dynamics by spatial integration of temporal fluctuations. *Nat. Commun.* **5**, 5123 (2014).
11. P. G. Debenedetti, F. H. Stillinger, Supercooled liquids and the glass transition. *Nature* **410**, 259–267 (2001).
12. P. W. Anderson, Through the glass lightly. *Science* **267**, 1615–1616 (1995).
13. McKenna, G. B.; Simon, S. L. 50th Anniversary perspective: challenges in the dynamics and kinetics of glass-forming polymers. *Macromolecules* **50**, 6333–6361 (2017).
14. J. Y. Ye, T. Hattori, H. Inouye, H. Ueta, H. Nakatsuka, Y. Maruyama, M. Ishikawa, Glass transition of associated solvents studied by fluorescence measurement of doped chromophores. *Phys. Rev. B* **53**, 8349–8353 (1996).
15. J. Y. Ye, T. Hattori, H. Nakatsuka, Y. Maruyama, M. Ishikawa, Microscopic dynamics of the glass transition investigated by time-resolved fluorescence measurements of doped chromophores. *Phys. Rev. B* **56**, 5286–5295 (1997).
16. http://polymerdatabase.com/polymer%20physics/Glass Transition.html (accessed April 8, 2020). In this site, we found an explanation that glass transition is pseudo-second Ehrenfest transition, or pseudo second-order transition.
17. E. Donth, "1. Introduction" and "2.1. The classical picture. No serious problem" in *The Glass Transition, Relaxation Dynamics in Liquid and Disordered Materials*, (Springer 2001), pp 1–66.
18. G. Jaegar, The Ehrenfest classification of phase transitions: introduction and evolution. *Arch. Hist. Sci.* **53**, 51–81 (1998).
19. H. E. Stanley, "What are the critical phenomena? A survey of some basic results" in *Introduction to phase transitions and critical phenomena*, (Oxford 1971), pp. 1–21.
20. C. A. Angell, K. L. Ngai, G. B. McKenna, P. F. McMillan, S. W. Martin, Relaxation in glassforming liquids and amorphous solids. *J. Appl. Phys.* **88**, 3113–3157 (2000).
21. K. Miyazaki, M. Ozawa, A. Ikeda, Recent development of theory of the glass transition. *Netsu Sokutei* **42**, 135–141(2015) (in Japanese).
22. H. Sillescu, Heterogeneity at the glass transition: a review. *J. Non-Cryst. Solids* **243**, 81–108 (1999).
23. Segment is a notion intrinsic to polymer physics and is not equivalent to monomer but means a moving body composed of one to ten monomers. Polymer dynamics based on statistical mechanics regards a polymer chain as an ensemble of segments for mathematical convenience, each of which can be treated statistically independent particles. Thus, we can treat polymer dynamics as micro Brownian motion.

24. M. D. Ediger, Spatially heterogeneous dynamics in supercooled liquids. *Annu. Rev. Phys. Chem.* **51**, 99–128 (2000).

25. K. Chibisov, G. V. Zakharova, H. Görner, Yu. A. Sogulyaev, I. L. Mushkalo, A. I. Tolmachev, Photorelaxation Processes in covalently linked indocarbocyanine and thiacarbocyanine dyes. *J. Phys. Chem.* **99**, 886–893 (1995).

26. H. Mori, Transport, collective motion, and Brownian motion. *Prog. Theor. Phys.* **33**, 423–455 (1965).

27. http://polymerdatabase.com/polymers/polyvinylacetate.html (accessed June 4, 2020). In this site we found that PVAC T_g ranges 297–315 K and 307 K is noted as a preferred value.

28. Y. Fuji-i, H. Morita, A. Takahara, T. Kanaya, "Mobility gradient of polystyrene in films supported on solid substrates" in *Glass transition, dynamics and heterogeneity of polymer thin films,* Ed. T. Kanaya (Springer, 2013), pp 1–28.

29. M. Beiner, J. Korus, H. Lockwenz, K. Schröter, E. Donth, Heat capacity spectroscopy compared to other linear response methods at dynamic glass transition in poly(vinyl acetate). *Macromolecules* **29**, 5183–5189 (1996).

30. H. Shimizu, "Kanwa-gensyo no kiso (Fundamentals in relaxation phenomena)" in *Kanwa-gensyo no kagaku* (*Relaxation phenomena in chemistry*), Eds. K. Higashi, S. Nagakura (Iwanami, 1973), pp 5–73 (in Japanese).

31. U. Tracht, M. Wilhelm, A. Heuer, H. Feng, K. Schmidt-Rohr, H. W. Spiess, Length scale of dynamic heterogeneities at the glass transition determined by multidimensional nuclear magnetic resonance. *Phys. Rev. Lett.* **81**, 2727–2730 (1998).

32. E. Hempel, G. Hempel, A. Hensel, C. Schick, E. Donth, Characteristic length of dynamic glass transition near T_g for a wide assortment of glass-forming substances. *J. Phys. Chem. B* **104**, 2460–2466 (2000).

33. F. Köhn, J. Hofkens, R. Gronheid, M. Van der Auweraer, F. C. De Schryver, Parameters influencing the on- and off-times in the fluorescence intensity traces of single cyanine dye molecules. *J. Phys. Chem. A* **106**, 4808–4814 (2002).

34. K. Jia, Y. Wan, A. Xia, S. Li, F. Gong, G. Yang, Characterization of photoinduced isomerization and intersystem crossing of the cyanine dye Cy3. *J. Phys. Chem. A* **111**, 1593–1597 (2007).

35. N. J. Turro,"Photophysical radiationless transitions" in *Modern Molecular Photochemistry* (Addison–Wesley, ed. 2, 1978), pp 153–198.

36. S. Yu. Grebenkin, B. V. Bol'shakov, Cage effects upon light irradiation on azo compounds: *cis → trans* isomerization in polymethyl methacrylate. *J. Photochem. Photobiol., A* **122**, 205–209 (1999).

37. Horizontally polarized excitation brought advantages over vertical polarization to collect more single-molecule fluorescence. This is consistent with previous findings,[33] showing 1.6-fold or more fluorescence photons by horizontally polarized excitation for cyanine dyes similar to Cy3. A possibility that Cy3 changes its absorption transition moment during the image acquisition in SMS cannot be totally ruled out. However, such possibility is likely quite small in our SMS with 36 ms resolution, in reference to the observation that less than 0.5% in all the analysis showed substantial absorption transition moment rotation for a cyanine dye similar to Cy3 embedded in a polymer at room temperature with 0.5–1.0 ms resolution.[33]

38. H. Mortazavian, C. J. Fennell, F. D. Blum, Structure of the interfacial region in adsorbed poly(vinyl acetate) on silica. *Macromolecules* **49**, 298–307 (2016).

SUPPORTING INFORMATION

Cosine and single exponential autocorrelation function derivation

We derive cosine waveform autocorrelation function and single exponential autocorrelation function from GLE in eq S1 using two approximations, respectively,[30] and finally point out two approximation difference in Figures S9A and S9B.

$$\frac{dA(t)}{dt} = i\omega_o A(t) - \int_0^t \varphi(t-t') A(t') dt' + f(t), \quad \text{(S1)}$$

where $A(t)$ means a dynamical variable, ω_o is formal angular frequency and zero in the present consideration, $f(t)$ is fluctuating external random force, and $\phi(t - t')$ is memory function,

$$\varphi(t-t') = \frac{\langle f(t)f(t')\rangle}{\langle A(0)A(0)\rangle}. \quad \text{(S2)}$$

The denominator in eq S3 can be changed into <$f(t)f(0)$> because $A(t)$, or $A(0)$ is any variable, including $f(t)$, or $f(0)$. Thus, eq S2 is converted into eqs 8 and S7. The integral in eq S1 indicates friction, or resistance against $A(t)$ by $f(t)$ in a general form. Deriving autocorrelation function in cosine or single exponential waveform depends on the approximation of the integral in eq S1. Before approximation, we convert eq S1 into

$$\frac{d}{dt}\langle A(t)A(0)\rangle = -\int_0^t \frac{\langle f(t)f(t')\rangle}{\langle A(0)A(0)\rangle}\langle A(t')A(0)\rangle dt' \quad \text{(S3)}$$

by substituting eq S2 into eq S1 and taking <$f(t)A(0)$> = <$f(t)$><$A(0)$> = 0. This equation comes from the fact that $f(t)$ and $A(0)$ are independent variables and < $f(t)$> = 0 due to randomly fluctuating $f(t)$. Dividing both sides in eq S3 by <$A(0)A(0)$> provides

$$\frac{d}{dt}\frac{\langle A(t)A(0)\rangle}{\langle A(0)A(0)\rangle} = -\int_0^t \frac{\langle f(t)f(t')\rangle}{\langle A(0)A(0)\rangle}\frac{\langle A(t')A(0)\rangle}{\langle A(0)A(0)\rangle} dt'. \quad \text{(S4)}$$

We then use an identity

$$\frac{\langle f(t)f(t')\rangle}{\langle A(0)A(0)\rangle} = \frac{\langle f(0)f(0)\rangle}{\langle A(0)A(0)\rangle}\frac{\langle f(t)f(t')\rangle}{\langle f(0)f(0)\rangle} \quad \text{(S5)}$$

and simplify eq S5 by the following definitions

$$\frac{\langle f(0)f(0)\rangle}{\langle A(0)A(0)\rangle} \equiv \omega^2 \quad \text{(S6)}$$

and

$$\frac{\langle f(t)f(t')\rangle}{\langle f(0)f(0)\rangle} \equiv \varphi(t-t'), \tag{S7}$$

where ω^2 is a constant and $\varphi(t-t')$ is a memory function involving $f(0)$ instead of $A(0)$ in eq S2. This replacement is valid considering that $A(t)$ means any dynamical variable.[26] We further define normalized autocorrelation function $\Phi(t)$ equivalent to $C(\tau)$:

$$\Phi(t) \equiv \frac{\langle A(t)A(0)\rangle}{\langle A(0)A(0)\rangle}. \tag{S8}$$

Thus, we simplified eq S4 into

$$\frac{d\Phi(t)}{dt} = -\omega^2 \int_0^t \varphi(t-t')\Phi(t')dt', \tag{S9}$$

which is equal to eq 9, finally providing cosine $\Phi(t)$ using $\varphi(t-t') = 1$.

Single exponential decay function $\Phi(t)$ depends on the approximation in eq S10 where $s = t - t'$ is used.

$$-\omega^2 \int_0^t \varphi(s)\Phi(s+t')ds =$$

$$-\omega^2 \Phi(t)\int_0^t \varphi(s)ds = -\omega^2 \Phi(t)\int_0^\infty \varphi(s)dt'. \tag{S10}$$

This approximation means extending the integral to infinity due to shorter $\varphi(s)$ duration compared with $\Phi(\underline{t})$, giving

$$\frac{d\Phi(t)}{dt} = -\gamma\Phi(t), \tag{S11}$$

where we set

$$\gamma \equiv -\omega^2 \int_0^\infty \varphi(s)ds \tag{S12}$$

From eq S11 we finally obtain normalized autocorrelation function showing single exponential decay,

$$\Phi(t) = \Phi(0)e^{-\gamma t}. \tag{S13}$$

Normalized autocorrelation function takes cosine waveforms under the approximation that memory function continues persistently, whereas memory function quick decay provides single exponential autocorrelation functions. We find the second approximation in primary Brownian motion consideration.
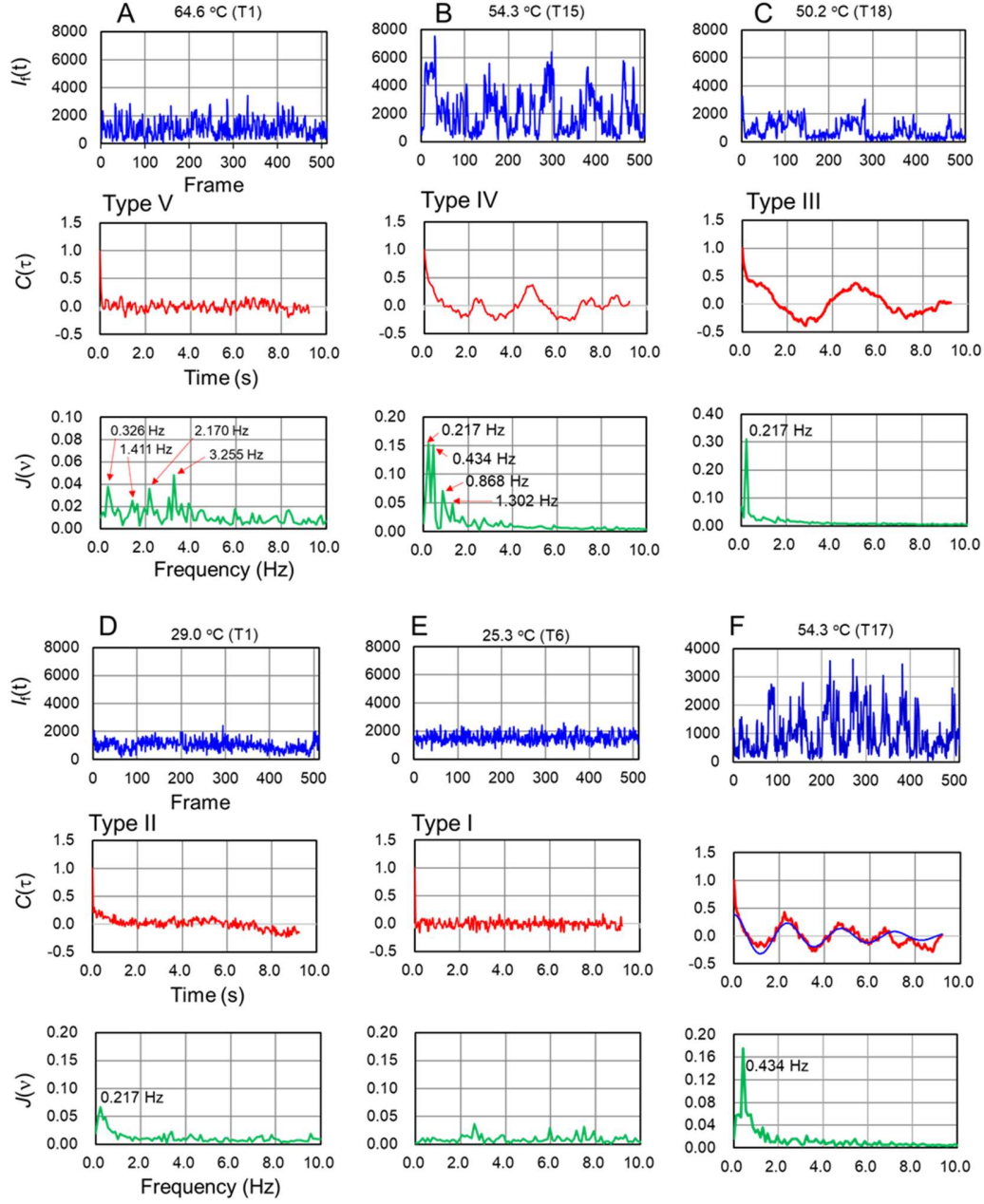
Figure S1. Representative fluorescence trajectories, $I_f(t)$; autocorrelation functions, $C(\tau)$; and power spectra $J(\nu)$. They were observed from single Cy3 molecules with PVAC overlay from cooling experiment (0.20–0.30 K /min) at (**A**) 64.6, (**B**) 54.3, (**C**) 50.2, (**D**) 29.0, (**E**) 25.3, and (**F**) 54.3 °C. Set (**F**) shows damped oscillation, which was fitted with a function $C(\tau) = C_0\exp(-t/C_1)\{C_2\cos(C_3t + C_4)\} + C_5$. We used a single exponential decay amplitude multiplied by one cosine function including distinct frequency 0.434 Hz in $J(\nu)$ as a single damped oscillator. The data in (**F**) presents difficulty in satisfactory fitting using a single frequency. Labels Type I to Type V are for $C(\tau)$ classification equal to those in Figure 3; Figure 4B and Table S1B summarize each type occurrences. Video images generating these data were captured with horizontally polarized excitation and averaged over 512 frames (36 ms/frame) followed by background subtraction.
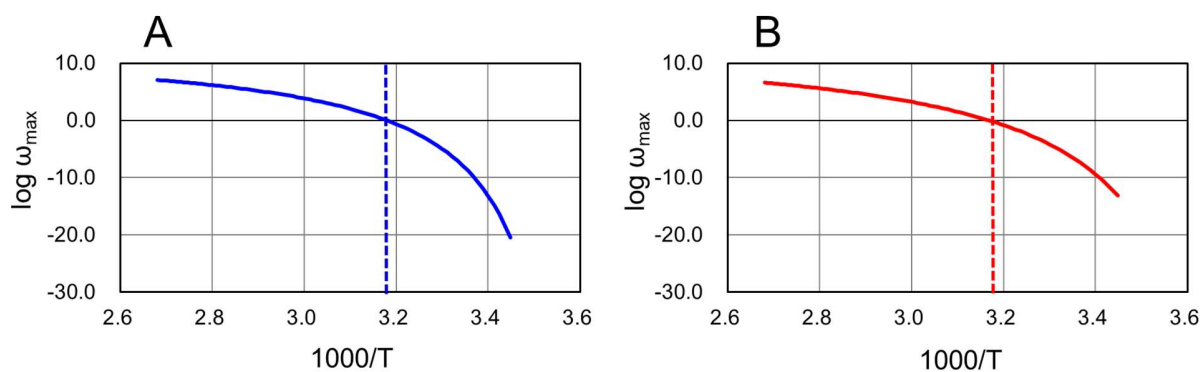
Figure S2. Temperature dependent PVAC resonance angular frequencies ω_{max}. They were observed by (**A**) shear modulus loss and (**B**) dielectric loss PVAC spectroscopy.[29] Parameters that reproduced each curve using eq 4 in (**A**) and (**B**) are B = 450 K, $T(\infty)$ = 276, and log ω_o = 11.7; B = 610 K, $T(\infty)$ = 266 K, and log ω_o = 12.3, respectively. Using the curves in (**A**) and (**B**), we obtained ω = 1.45 rad/s, or ν = 0.231 Hz and ω = 0.710 rad/s, or ν = 0.113 Hz, respectively at T = 315 K (42 °C), or $1000/T$ = 3.17 (drawn with broken lines).
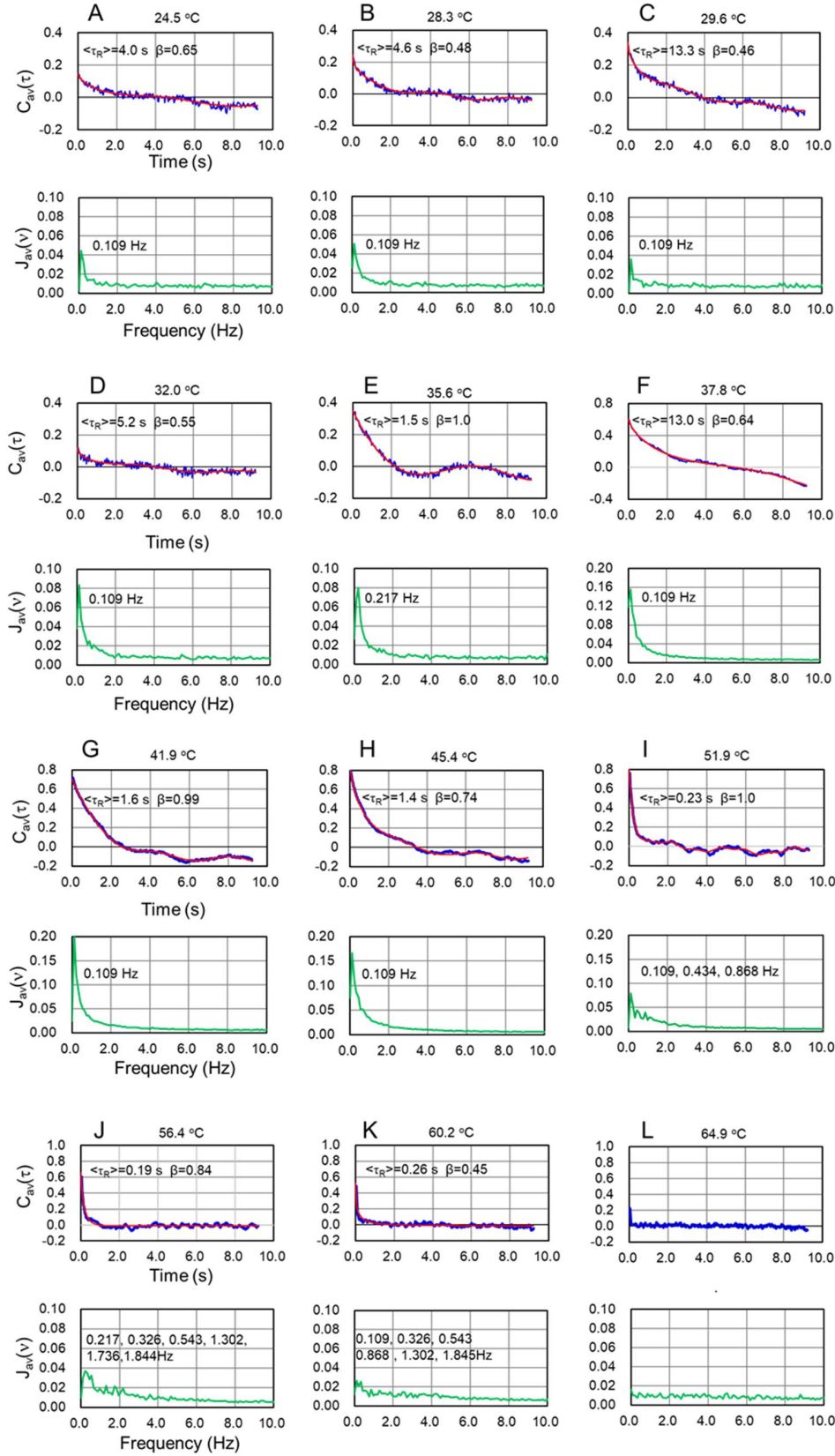
Figure S3. Average autocorrelation functions, $C_{av}(\tau)$ and power spectra, $J_{av}(v)$. They were observed for heating (0.2 K /min) from single Cy3 molecules with PVAC overlay and computed from twenty single Cy3 molecules free from photobleaching at (**A**) 24.5, (**B**) 28.3, (**C**) 29.6, (**D**) 32.0, (**E**) 35.6, (**F**) 37.8, (**G**) 41.9, (**H**) 45.4, (**I**) 51.9, (**J**) 56.4, (**K**) 60.2, and (**L**) 64.9 °C. In (**L**), $<\tau_R>$ evaluation was halted due to inability to identify decay in $C_{av}(\tau)$. Each $C_{av}(\tau)$ curve except for (**L**) was fitted with eq 2 and includes calculated curve in a red line and parameters $<\tau_R>$ and β.
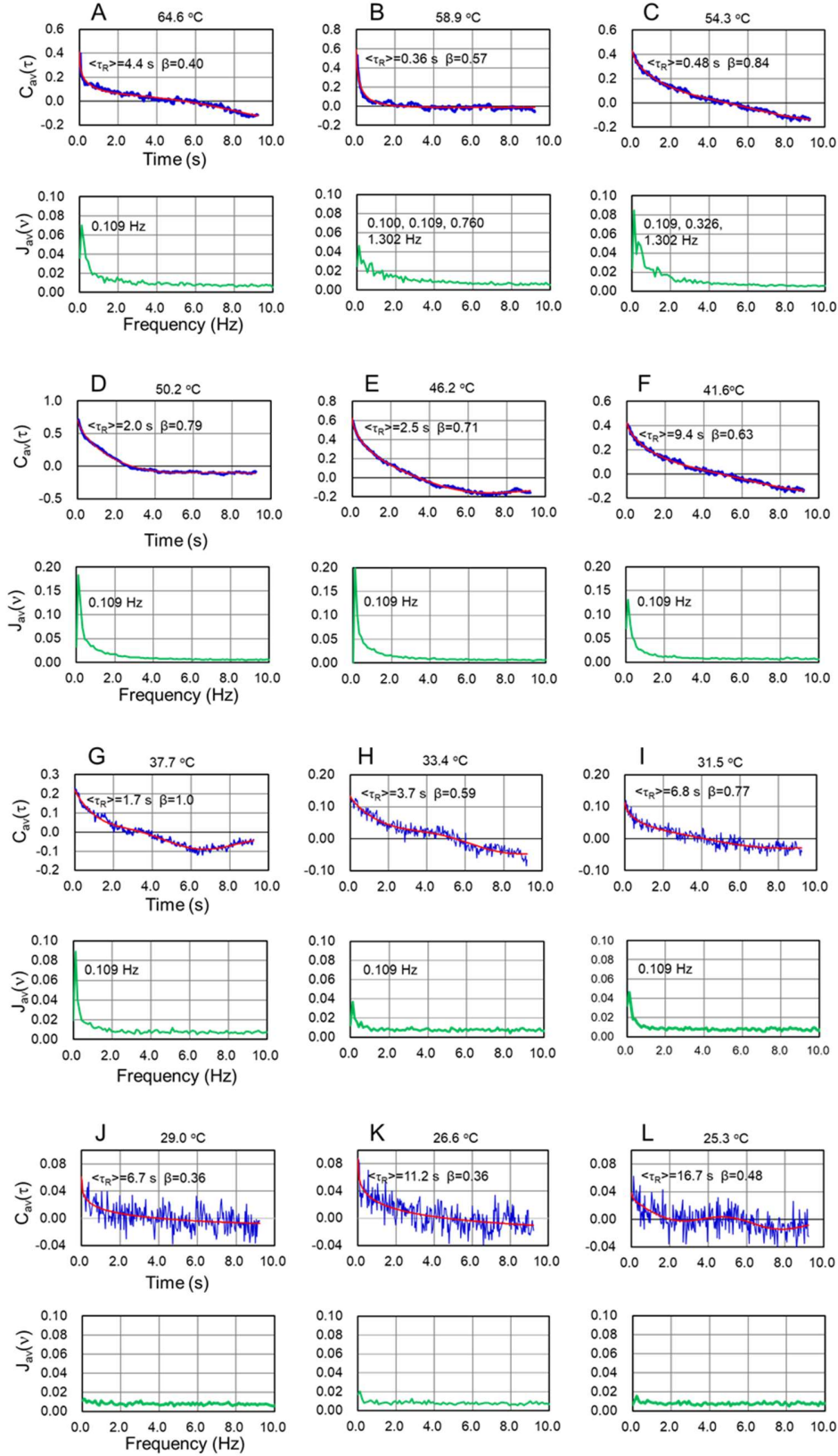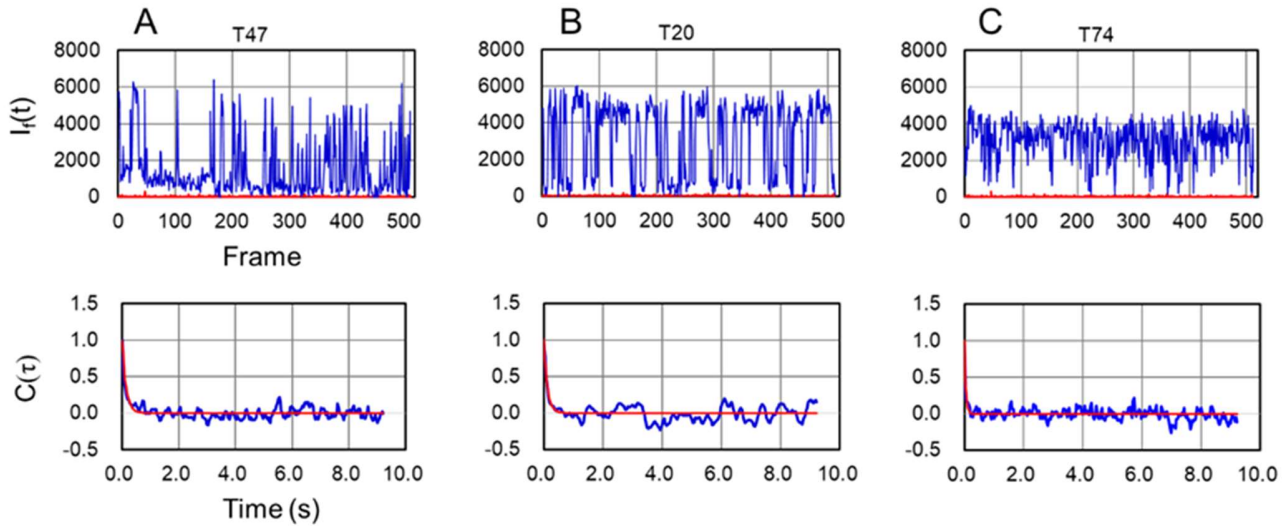
Figure S4. Average autocorrelation functions, $C_{av}(\tau)$ and power spectra, $J_{av}(v)$. They were observed for cooling (0.2–0.3 K/min) from single Cy3 molecules with PVAC overlay and computed from twenty single Cy3 molecules free from photobleaching at (**A**) 64.6, (**B**) 58.9, (**C**) 54.3, (**D**) 50.2, (**E**) 46.2, (**F**) 41.6, (**G**) 37.7, (**H**) 33.4, (**I**) 31.5, (**J**) 29.0, (**K**) 26.6, and (**L**) 25.3 °C. Each $C_{av}(\tau)$ curve was fitted with eq 2 and includes calculated curve in a red line and parameters $\langle\tau_R\rangle$ and β.
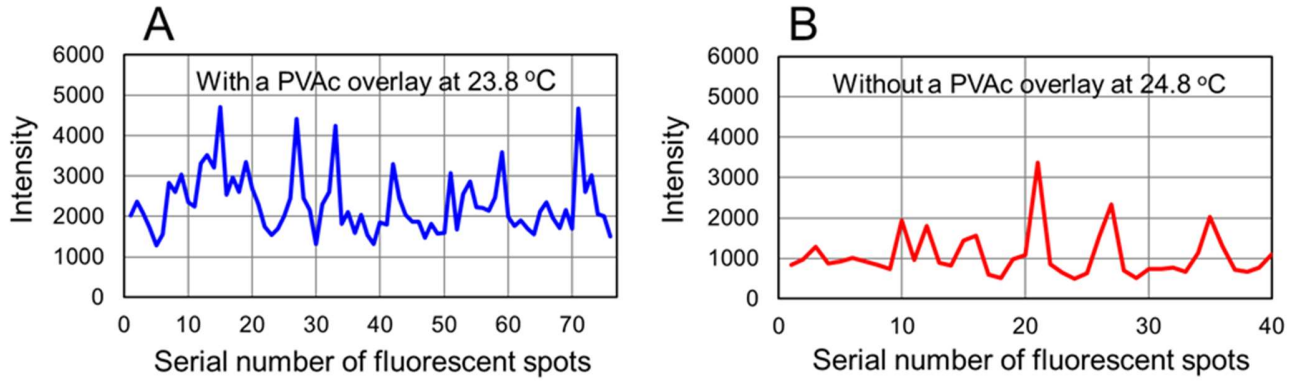
Figure S5. Fluorescence intensity distribution from single Cy3 molecules. They were observed (**A**) with and (**B**) without PVAC overlay at room temperature (23.8 and 24.8 °C, respectively). Video images generating these data were captured with circularly polarized excitation and averaged over 512 frames (36 ms/frame) followed by background subtraction. Average intensity was 2318 ± 759 and 1072 ± 574 for (**A**) and (**B**), respectively, providing intensity ratio 2.16.

Figure S6. Representative fluorescence trajectories, $I_f(t)$ and autocorrelation functions, $C(\tau)$ fitted with single exponential decay functions using samples without PVAC overlays. They were observed from single Cy3 molecules at 22.1 °C, showing (**A**) 0.137, (**B**) 0.117, and (**C**) 0.0456 s lifetime τ_R, respectively. Each $C(\tau)$ was fitted with a single exponential function (red curve). Video images generating these data were captured with horizontally polarized excitation and averaged over 512 frames (36 ms/frame) followed by background subtraction.
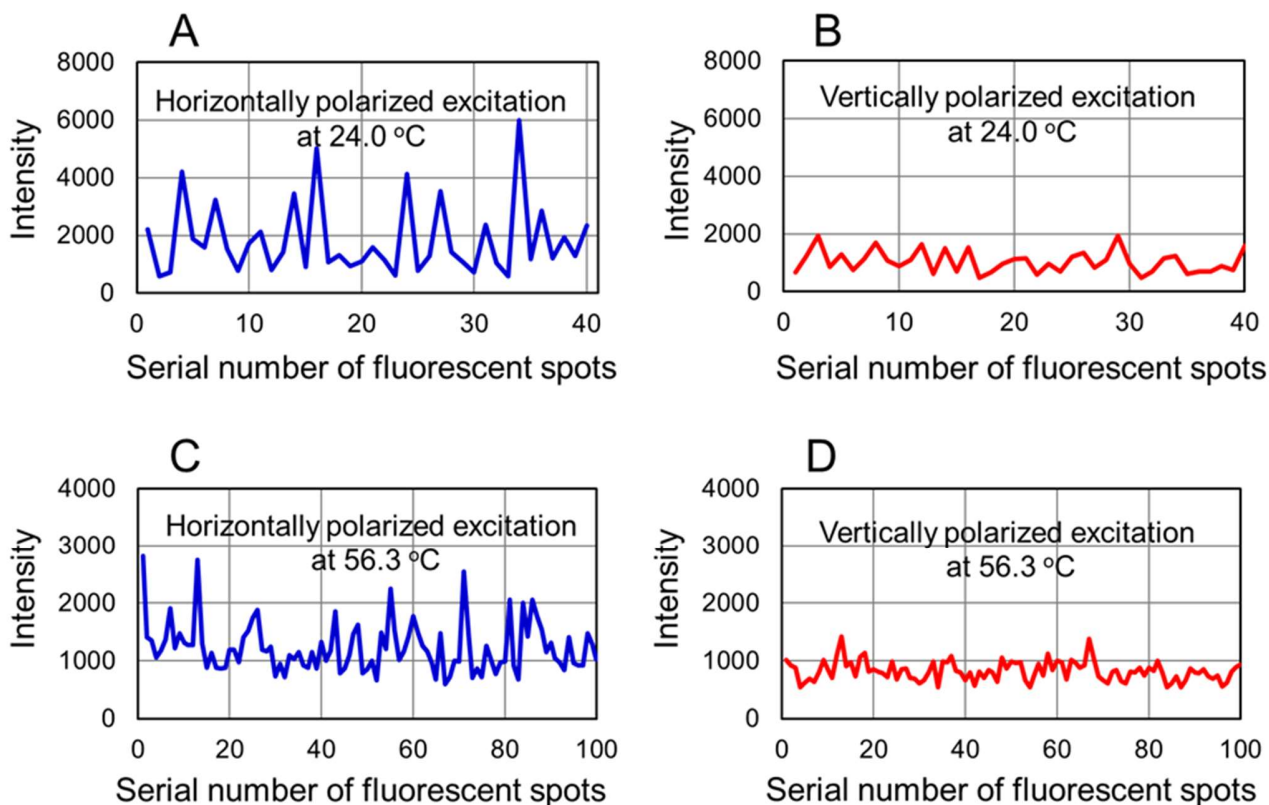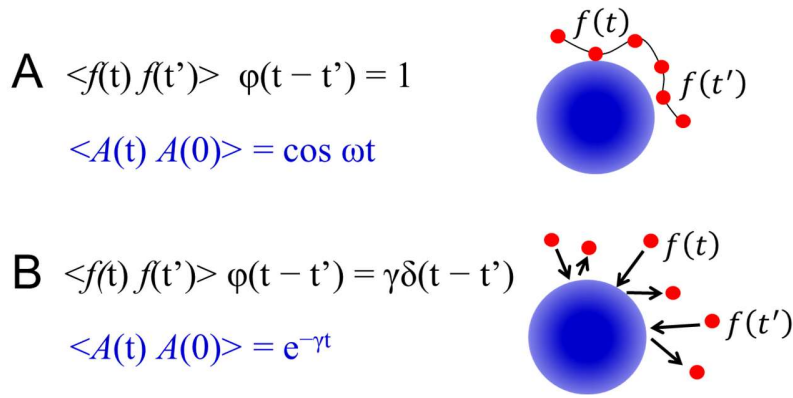
Figure S7. Excitation polarization and temperature dependent fluorescence intensity distribution using samples with PVAC overlays. They were observed from single Cy3 molecules by (**A**) horizontally (in parallel with the sample surface) and (**B**) vertically polarized excitation at 24.0 °C on the same field of view; (**C**) horizontally and (**D**) vertically polarized excitation at 56.3 °C on the same field of view. Video images were captured by changing field of view between 24.0 and 56.3 °C to minimize photobleaching and averaged over 512 frames (36 ms/frame) followed by background subtraction. For (**A**) and (**B**), average fluorescence intensity was 1840 (standard deviation 1287) and 1037 (standard deviation 388) for horizontal and vertical excitation, respectively (intensity ratio 1.77); for (**C**) and (**D**), average intensity was 1233 ± 435 and 824 ± 181 for horizontal and vertical excitation, respectively (intensity ratio 1.50).
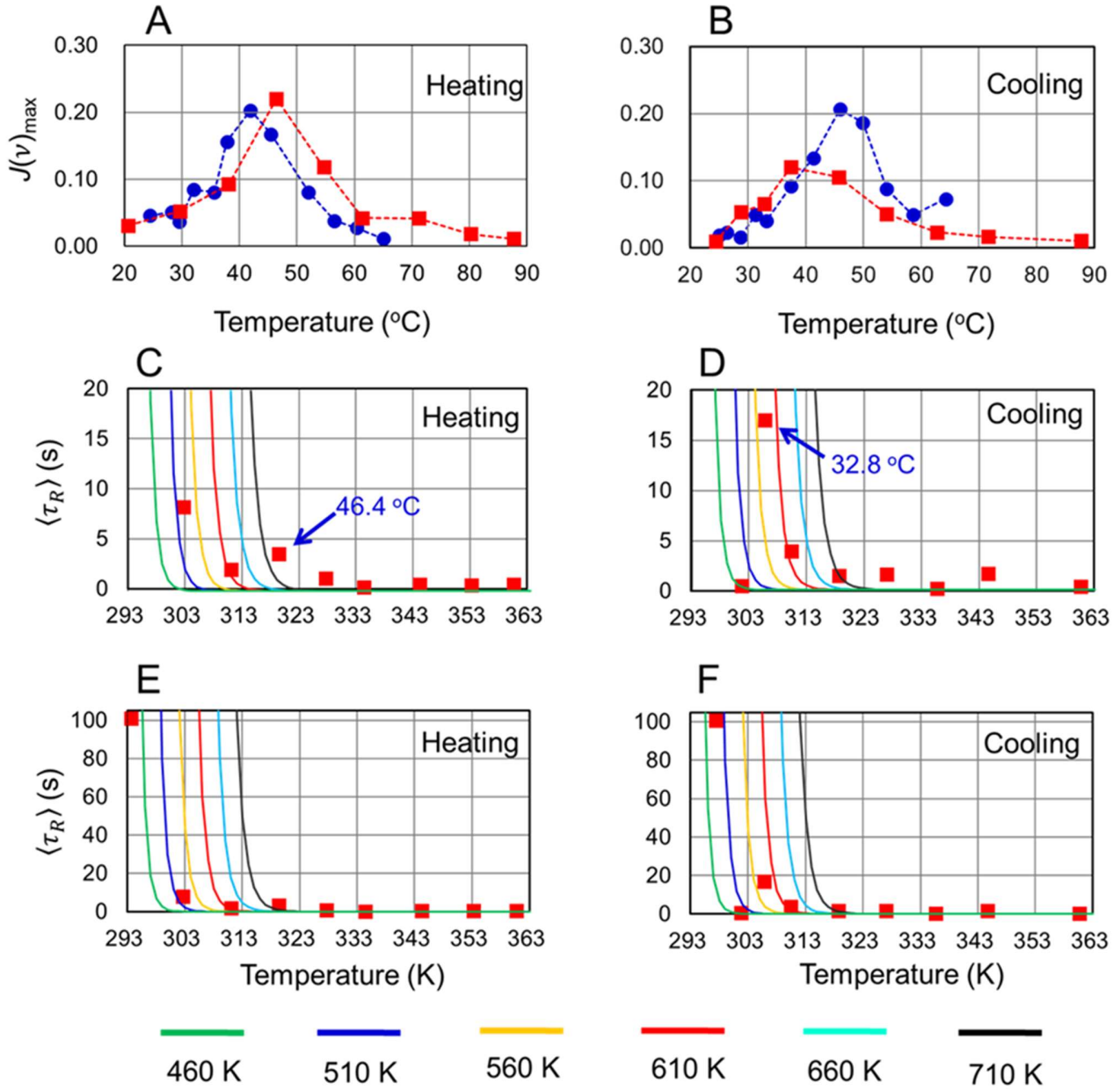
Figure S8. Temperature dependent maximum average power spectra, $J_{av}^{max}(\nu)$ and average relaxation times, $\langle\tau_R\rangle$. $J_{av}^{max}(\nu)$ for (**A**) heating and (**B**) cooling (red filled squares), superposed with $J_{av}^{max}(\nu)$ for heating and cooling in Figures 5A and 5B (blue filled circles), respectively. We computed $\langle\tau_R\rangle$ from $C_{av}(\tau)$ averaged over thirty $C(\tau)$ for (**C**) heating and (**D**) cooling. (**E**) and (**F**) are presented with extended $\langle\tau_R\rangle$ scale 0–100 s for (**C**) and (**D**), respectively. In (**C**)–(**F**) $\langle\tau_R\rangle$ is superposed with VFT lines (B = 460, 510, 560, 610, 660, and 710 K in green, blue, orange, light blue, and gray, respectively) computed using eq 4. Three VFT lines for B = 610, 660, and 710 K were experimentally identified.[29] Two arrows in (**C**) and (**D**) specify data points giving cusp-shaped discontinuous transitions. The heating and cooling experiment were carried out using the same sample (heating and cooling rate, 1.0 K /min).

A $\langle f(t) f(t')\rangle \; \varphi(t - t') = 1$

$\langle A(t) A(0)\rangle = \cos \omega t$

B $\langle f(t) f(t')\rangle \; \varphi(t - t') = \gamma \delta(t - t')$

$\langle A(t) A(0)\rangle = e^{-\gamma t}$

Figure S9. Two GLE approximations. (**A**) No memory function $\varphi(t - t')$ extinction generates continuum fluid-like external forces $f(t)$ and $f(t')$ picture. This means permanent correlation between $f(t)$ and $f(t')$ even for $t \neq t'$, providing cosine $\langle A(t)A(0)\rangle$ waveform. (**B**) Instantaneous $\varphi(t - t')$ extinction characterizes scattered particle-like external forces $f(t)$ and $f(t')$ picture. This shows no correlation between $f(t)$ and $f(t')$ for $t \neq t'$ characterized by delta function $\delta(t - t')$, leading to single exponential $\langle A(t)A(0)\rangle$ decay.

Table S1A. $C(\tau)$ waveform classification for heating experiments

	Type I	Type II	Type III	Type IV	Type V
24.5 ℃	65%	25%	10%	0.0%	0.0%
28.3 ℃	40%	25%	10%	0.0%	0.0%
29.6 ℃	44%	50%	0.0%	6.0%	0.0%
32.0 ℃	32%	42%	26%	0.0%	0.0%
35.6 ℃	29%	18%	53%	0.0%	0.0%
37.8 ℃	0.0%	17%	83%	0.0%	0.0%
41.9 ℃	0.0%	10%	90%	0.0%	0.0%
45.4 ℃	0.0%	5.0%	95%	0.0%	0.0%
51.9 ℃	5.0%	0.0%	25%	70%	0.0%
56.4 ℃	0.0%	15%	10%	65%	10%
60.2 ℃	5.0%	0.0%	0.0%	27%	68%
64.9 ℃	0.0%	0.0%	0.0%	12.0%	88%

Table S1B. $C(\tau)$ waveform classification for cooling experiments

	Type I	Type II	Type III	Type IV	Type V
25.3 ℃	84%	16%	0.0%	0.0%	0.0%
26.6 ℃	80%	20%	0.0%	0.0%	0.0%
29.0 ℃	90%	5.0%	0.0%	5.0%	0.0%
31.5 ℃	60%	25%	15%	0.0%	0.0%
33.4 ℃	65%	30%	5.0%	0.0%	0.0%
37.7 ℃	45%	25%	30%	0.0%	0.0%
41.6 ℃	30%	30%	40%	0.0%	0.0%
46.2 ℃	10%	20%	50%	20%	0.0%
50.2 ℃	0.0%	15%	75%	10.0%	0.0%
54.3 ℃	0.0%	5.0%	55%	35%	5.0%
58.9 ℃	10%	20%	20%	35%	15%
64.6 ℃	16%	37%	0%	10.0%	37%

26